

Experimental Study on the Dilatancy and Fracturing Behavior of Soft Rock Under Unloading Conditions

Xing Huang¹ · Quansheng Liu^{1,2} · Bin Liu¹ · Xuewei Liu¹ · Yucong Pan¹ · Jianping Liu¹

Received: 1 August 2016 / Revised: 25 December 2016 / Accepted: 30 December 2016 / Published online: 1 March 2017
© Iran University of Science and Technology 2017

Abstract To reveal the deformation mechanism during tunneling in deep soft ground, triaxial unloading confining pressure tests and triaxial unloading creep tests were carried out on sandy mudstone specimens to study the dilatancy and fracturing behavior of soft rock. In the triaxial unloading confining pressure tests, the stress path and different unloading rates were considered to reflect the unloading characteristics of the excavation methods. The unloading rate effects and the rock damage evolution law are studied. The following conclusions are obtained from the results. Firstly, when the unloading rate is smooth, the peak strengths and deviatoric stress–strain curves under the unloading condition are close to those under the conventional loading condition. Secondly, the post-peak

brittle characteristics are more apparent with the increasing unloading rates. Thirdly, the soft rock undergoes five deformation and failure regimes of elasticity, pre-peak unloading damage–dilatancy, post-peak brittle drop, linear strain softening and residual perfect plasticity under quasi-static smooth unloading of mechanized excavation which is mainly focused on in this study. Fourthly, the damage evolution law at the pre-peak damage–dilatancy stage follows an exponential function. Fifthly, during the post-peak stages, multistage microfractures are initiated, propagated and finally coalesced forming a shear-fragmentation band with a certain thickness, accompanied by significant volumetric dilatancy. In the triaxial unloading creep tests, multistep unloading of the confining pressure was applied, while the axial pressure was kept constant. The results show that when the deviatoric stress is larger and the experienced creep time is longer, the unloading effect and creep characteristics become more apparent accompanied with obvious lateral dilatancy, eventually leading to significant creep–dilatancy. The progressive failure with time is caused by the damage accumulating with time-dependent crack expansion, which can be called as ‘time-dependent damage and fracturing’. The reasons for the above evolution process are presented, then the deformation mechanism of soft rock is revealed. The soft rock deformation mainly consists of two parts. One part is the pre-peak damage–dilatancy and post-peak fracture–bulking produced at the excavation unloading instant. The other part is creep–dilatancy caused by time-dependent damage and fracturing in a period of time after excavation. The above-mentioned results of damage, dilatancy and fractures evolution process are in good agreement with the in situ monitoring results and previous studies about the surrounding rock convergence, fracturing and EDZ (excavation damaged zone) development.

✉ Quansheng Liu
liuqs@whrsm.ac.cn

Xing Huang
huangxing220808@163.com

Bin Liu
liubin@whrsm.ac.cn

Xuewei Liu
liuxw87@126.com

Yucong Pan
pyc1991@whu.edu.cn

Jianping Liu
18071045126@189.cn

¹ State Key Laboratory of Geomechanics and Geotechnical Engineering, Institute of Rock and Soil Mechanics, Chinese Academy of Sciences, Shuiguohu Street, Wuchang, Wuhan 430071, People’s Republic of China

² Key Laboratory of Geotechnical and Structural Engineering Safety of Hubei Province, School of Civil Engineering, Wuhan University, Wuhan 430072, People’s Republic of China

Keywords Unloading · Damage–dilatancy · Fracture–bulking · Time-dependent damage and fracturing · Creep–dilatancy · Deformation mechanism

1 Introduction

Currently, a growing number of tunnels and roadways are constructed in deep locations [1]. However, soft and weak grounds with high in situ stress widely exist in deep long tunnels. The high geostress and weak structures of deep soft ground constitute the basic conditions of squeezing and large deformation [2, 3]. Severe squeezing and large deformation will result in the construction being unsafe or serious hazards, such as inadmissible convergence, surrounding rock instability, overloading on lining, schedule delay and huge economic losses [4, 5]. For instance, during tunnel boring machine (TBM) tunneling, the cutter head, shield and backup systems are vulnerable to trapping or jamming when squeezing and large deformation are produced [6, 7]. Additionally, soft rock has significant time-dependent properties [3, 8, 9]. For example, during the Venezuela Yacambú–Quibor Tunnel construction and the Italian Nuovo Canale Val Viola Tunnel construction, the TBMs were jammed during the holidays [5, 10]. Thus, a clear understanding of the soft rock deformation mechanism is significantly important for ensuring construction safety.

The deformation mechanism of soft rock in previous literature can be summarized as: complete shear failure [4], yield failure [11], shear-slip failure [11], time-dependent microfracturing [12] and stress relaxation of foliated rock [13]. For example, Aydan [11] examined the soft rock deformation as elastic, plastic and viscous behavior, and divided the failure patterns into pure shear failure, bending failure, tensile-shear fracturing and sliding failure. Whereafter more and more researchers [14–16] took the rock deformation and failure as the result of damage and cracking which result in volume expansion. A large number of previous studies [17–20] have shown that the stress-induced instability, squeezing and large deformation of soft rock are mainly the results of the dilatancy and fracturing behavior, such as the pre-peak damage, microcrack initiation, crack extension and fracture coalescence.

Many researchers have performed experimental studies [21, 22] to analyze the rock dilatancy and fracturing mechanism. However, most of the previous experimental studies [22] usually adopted a continuous loading approach, under which the damage–dilatancy and post-peak failure behavior of the rock were quite different from those during underground excavation, where the surrounding rock is always under an unloading confining pressure state. A great number of studies have demonstrated that the rock mechanical

behaviors and deformation characteristics are significantly associated with stress history, stress path and loading rates [23–27]. Kaiser [23] have showed that both of the directions and values of the principle stresses change during excavation and mining by in situ monitoring, and the stress path has evident impact on the excavation stability. Eberhardt [28] have found that the principal stress magnitude and orientation vary with the progressive advancement of the tunnel face by 3D numerical simulation. Martin [29] and Cai and Kaiser [30] have also pointed out that the stress change and the principal stress rotation during excavation are the major reasons of rock strength loss and failure. According to the elasto-plastic theory [31], because of the different internal variables' evolution process between the loading and unloading stress paths, there are many differences in the strength and deformability and the rocks show quite different deformation and failure characteristics under the two stress paths. It is generally believed that the radial stress (corresponding to the confining pressure) of the surrounding rock always decreases during excavation. Qiu [15], Huang [18] and Zhao [22] et al. carried out unloading tests to study the damage, failure properties and constitutive models, which are meaningful to understand the rock response under unloading conditions. However, previous experimental tests and theoretical models corresponding to surrounding rock under confining pressure unloading state are few. Furthermore, previous unloading experimental studies rarely reflect the natural unloading characteristics of the excavation methods. Thus, the deformation and dilatancy properties under excavation unloading conditions cannot be understood clearly. So, it is of vital importance to perform unloading tests, in which the stress path and unloading rates reflect the unloading features of the excavation methods, the conclusions based on which are more accurate for capturing the rock damage, dilatancy and fracture evolution process.

Generally, the rheological properties of the soft rock is much more remarkable than those of other rocks [8, 32]. Thus, special attention should be paid to the temporal properties of the soft surrounding grounds during the construction stoppage time, such as TBM standstills, holidays or tunnel service life. The studies about the creep characteristics of the soft rock, especially the time-dependent dilatancy and fractures evolution, have significant importance in analyzing and predicting the relatively long-term surrounding rock stability [33]. Laboratory rheological testing is a useful means to investigate the creep behavior under different stress conditions, based on which creep constitutive models can be set up and the corresponding creep parameters can be obtained to capture the time-dependent behaviors of soft rock. For example, Zhao et al. [34] performed creep experiments under circular increment step load and unload on soft ore rock in Jinchuan Mine III, and

established a nonlinear viscoelastic–plastic creep model. Debernardi and Barla [35] put forward a new viscoplastic model (SHELVIP model) for design analysis of tunnels in squeezing conditions, and fitted the model with the triaxial creep tests. Wang et al. [36] performed triaxial destructive creep–damage tests using quasi-static loading on rock salt specimens to study its creep–damage–rupture behavior. However, many of the previous researches ignored the unloading effects on the creep process, and the damage, dilatancy and fracturing characteristics were not studied in deep. So, it is necessary to carry out unloading creep tests with high initial confining pressure to study the time-dependent dilatancy and fracturing behavior of soft rock.

Therefore, triaxial unloading confining pressure tests and triaxial unloading of confining pressure creep tests are carried out with deep soft rock specimens in this study. The triaxial unloading tests reflect the unloading characteristics of tunneling methods (this paper mainly focuses on the quasi-static mechanized tunneling), and the triaxial unloading creep tests reflect the time-dependent characteristics. Based on the testing results, the dilatancy and fracturing behavior under different stress states are obtained. Furthermore, the deformation mechanism of soft rock is revealed. The research results will have meaningful guide for tunnel stability analyses and control.

2 Laboratory Investigation on the Dilatancy and Fracturing Behavior after Excavation via Triaxial Unloading Confining Pressure Tests

2.1 The Unloading Characteristics of Underground Tunneling

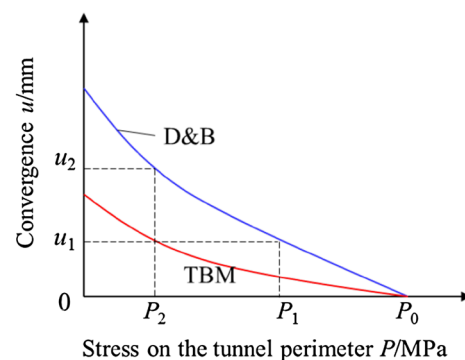
Currently, there are primarily two types of underground excavation methods: the drill-and-blast (D&B) method and the mechanized excavation method (e.g., TBM tunneling). Previous studies have shown that the surrounding ground disturbance is significantly influenced by the excavation methods and the stress release modes [37].

When excavated via the drill-and-blast (D&B) method, the crack surfaces of adjacent holes connect mutually in tens of milliseconds after the blasting, and the normal stresses on these crack surfaces are removed when the cracks are connected [38]. The disturbance of surrounding rock is strongly influenced by the blasting loads and high-speed dynamic unloading effects [39], which is dramatically different from quasi-static unloading.

The stress adjustment procedure and rock response under the mechanized method such as TBM tunneling are quite different from those under the drill-and-blast method. The TBM overcut cutters, which are at the cutter head outer periphery, roll and fragment the rock around

the tunnel. There is an angle between the overcut cutters and the normal face of the cutter head. The following phenomena are observed: the initial geostress smoothly transforms into secondary stresses, the confining pressure is unloaded gradually for a long time, and the stored energy is released gradually. The stress–strain curves and disturbance stress curves of the surrounding rock show good continuity and transition [40]. The stress–convergence relationship of the surrounding rock under the TBM and D&B excavation methods are shown in Fig. 1. It can be concluded that the stress releases gently and the excavation disturbance is smaller under mechanized tunneling (e.g., TBM tunneling).

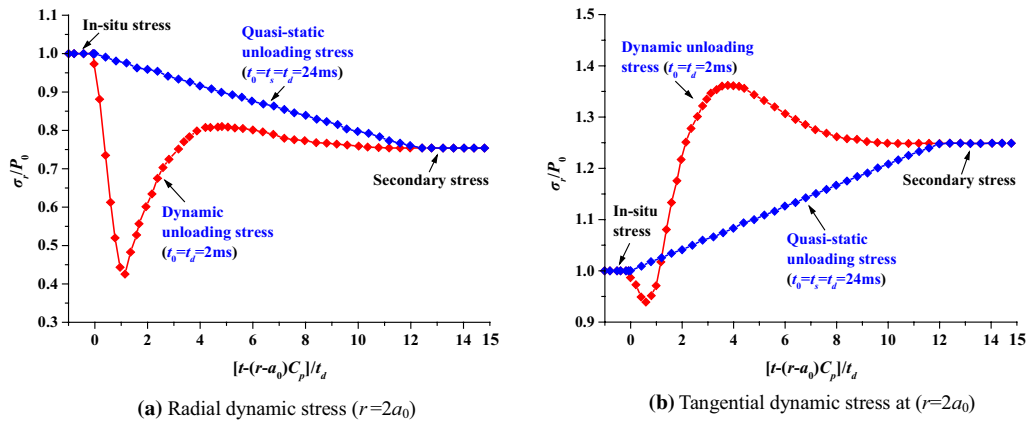
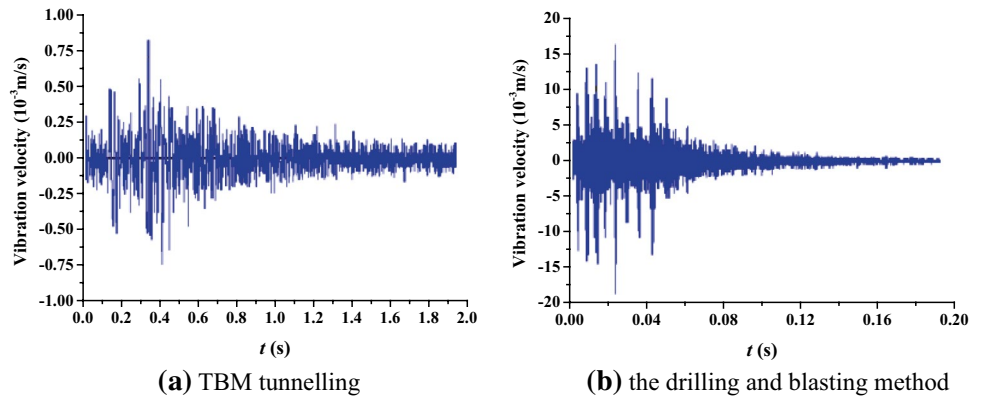
The unloading characteristics induced by the two excavation methods are significantly different. Figure 2 shows the surrounding rock vibration curves under the mechanized excavation (TBM) and drill-and-blast method at the diversion tunnels of the Jinping-II Hydropower Station (China). It is observed that the stress waves during TBM tunneling are gentler than those under the drill-and-blast method. Specifically, the vibration amplitudes during TBM tunneling are very small, with a peak amplitude of 1 mm/s. Yan [41] assumed that the surrounding rock masses obey the linear elastic constitutive model and then obtained the analytical solutions for the stress adjustment procedure under the two excavation methods via Laplace transforms and the integral approach, as shown in Fig. 3. Under dynamic unloading, the following phenomena are observed: (1) the radial stress rebounds quickly; (2) the tangential dynamic stress concentrates; and (3) the radial and tangential stresses of the rock mass first increase, then decrease and finally converge to secondary stresses. Under smooth quasi-static unloading, the stresses near the excavation contour transform from the initial to the secondary stress state smoothly. In conclusion, the



Where P_0 is the initial geostress; P_1 and P_2 are the redistributed secondary stress; u_1 and u_2 are the corresponding convergence on the excavation boundary.

Fig. 1 Stress–convergence relationship of the surrounding rock under TBM and D&B excavation

Fig. 2 Vibration velocity of the surrounding rock under different tunneling methods at the diversion tunnels at Jinping-II Hydropower Station (China). **a** TBM tunnelling, **b** the drilling and blasting method



where, the vertical coordinates σ_r/P_0 and σ_{θ}/P_0 represents the ratios between radial and tangential dynamic stresses to the in-situ stress respectively; a_0 is the excavation radius; C_p is the longitudinal wave velocity; t_d is the unloading time; the horizontal ordinate $[t-(r-a_0)C_p]/t_d$ represents the zeroization and dimensional normalization of stress propagation time.

Fig. 3 Quasi-static and dynamic unloading stress fields [41]. **a** Radial dynamic stress ($r = 2a_0$), **b** tangential dynamic stress at ($r = 2a_0$)

surrounding rock experiences dramatically different stress paths between the TBM (smooth quasi-static unloading) and drill-and-blast method (sudden dynamic unloading). Additionally, Cai [37] has calculated the influences of the sudden (drill-and-blast method) and quasi-static (corresponds to TBM tunneling) stress adjustment on excavation damage zone. The calculations showed that tunneling methods significantly affected the excavation response, and the disturbance was much smaller under quasi-static unloading.

The quasi-static unloading process is generally used in the study of the properties of the surrounding rock under unloading conditions. For instance, Liu and Li [42] analyzed the tunneling disturbance characteristics using quasi-static unloading.

Therefore, it can be concluded that the mechanized excavation (TBM) on the excavation contour is a smooth quasi-static unloading process. For a deep buried tunnel, the unloading characteristics of mechanized excavation (TBM)

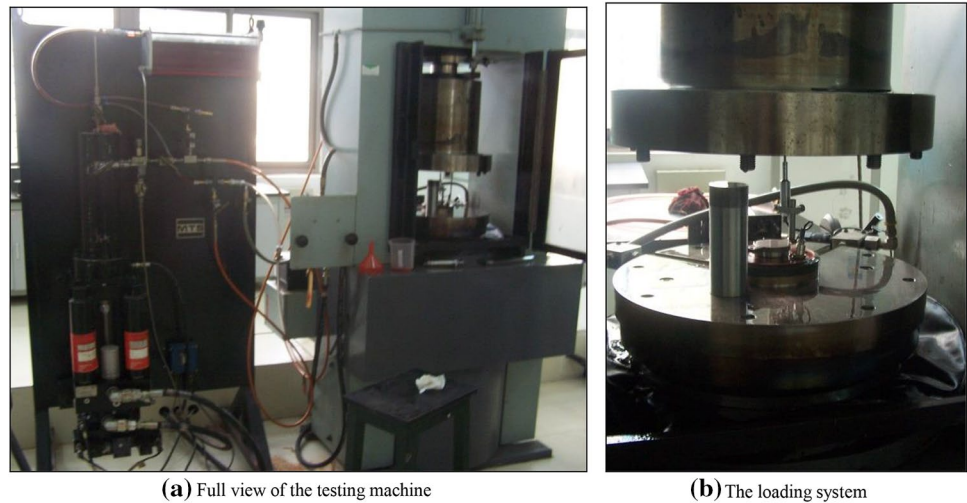
is a smooth quasi-static unloading with high initial confining pressure.

The stress path has significant influences on the rock mechanical behavior, which has aroused wide attention [24, 43]. However, the mechanical behavior of deep soft rock under smooth quasi-static excavation unloading with high initial geostress needs further study. Therefore, smooth quasi-static unloading condition (e.g., during TBM tunneling) is focused on in the study of the transient dilatancy and fracturing behavior of deep soft ground, while the response under dynamic unloading and blasting loads in not discussed here.

2.2 Testing Methodology

In this section, the triaxial unloading confining pressure tests were performed to study the instantaneous deformation and failure behavior of soft rock after excavation.

Fig. 4 MTS 815.03 servo-controlled rock mechanics testing machine. **a** Full view of the testing machine, **b** the loading system



2.2.1 Testing Apparatus

Triaxial compression tests and triaxial unloading confining pressure tests were carried out using an MTS815.03 electro-hydraulic servo-controlled rock mechanics testing machine (Fig. 4). This apparatus is composed of servo-controlled automatic triaxial loading, measuring and control systems. The MTS testing system is equipped with an excellent program control function. Different testing methods and loading models can be performed by the management software. Uniaxial and triaxial compression tests, pore water pressure tests and water permeability tests can be carried out in this testing system.

2.2.2 Rock Specimens

The cylindrical rock samples used for the tests were sandy mudstone cored from a –848 m mechanized excavation rail roadway in the Huainan Panyidong Coal Mine (China) with a buried depth of 1020 m. There is another coal mine named Huainan Zhangji, in the neighborhood of Panyidong coal mine, and both are located in the same Huainan mining area (China). The 1413 and 1415 A Methane Gas Extraction Roadways in the Zhangji coal mine were constructed using a gripper TBM that was developed by Northern Heavy Industries Group Co. Ltd. (China) [1]. The –848 m rail roadway in the Huainan Panyidong coal mine was mechanized and excavated by a cantilever-type road header. The two roadways have similar unloading characteristics (quasi-static smooth unloading). In addition, their surrounding grounds are both buried in the same strata, sandy mudstone formations, which have similar geological conditions and geostress situations. Because the TBM advance rate is fast, the corresponding support installation is also rapid, and there is rarely a space that can be used for drilling rock

samples. Even if there is space, drilling is also very difficult to perform especially in shielded TBM tunnels due to the restriction of segmental lining and other mechanical equipment. We tried to drill rock samples from the TBM water diversion tunnels at the Jilin Songhua River (China) and Lanzhou Water Source Project (China), but the rock samples were difficult to drill. Thus, it is difficult to drill rock specimens in other TBM tunnels. The rock samples that cored from the Panyidong coal mine can represent the typical deep soft rock characteristics.

The stress–strain curves and the basic mechanical parameters of the uniaxial and conventional triaxial compression tests of sandy mudstone are shown in Fig. 5 and Table 1. From these, it can be seen that sandy mudstone is a type of typical soft rock. The size of the specimens is $\Phi 50 \times H100$ mm, the machining accuracy of which is in accordance with the approaches suggested by the International Society for Rock Mechanics (ISRM) [44].

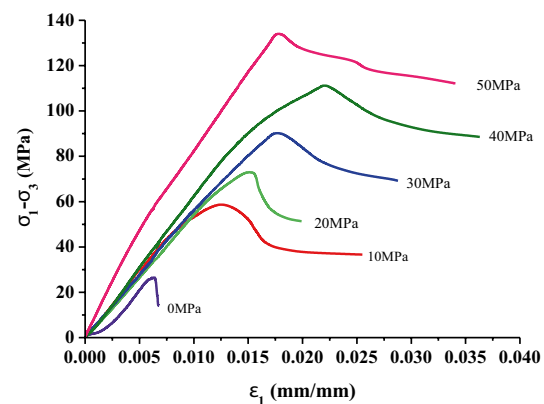


Fig. 5 Deviatoric stress ($\sigma_1 - \sigma_3$)~axial strain ϵ_1 curves from conventional triaxial compression tests

Table 1 Triaxial compression test results of sandy mudstone

| Confining pressure σ_3 /MPa | Peak strength σ_{1m} /MPa | Axial strain at peak strength $\epsilon_{1m}/10^{-3}$ | Lateral strain at peak strength $\epsilon_{3m}/10^{-3}$ | Volumetric strain at peak strength $\epsilon_{vm}/10^{-3}$ | Elastic modulus E /GPa | Poisson's ratio μ |
|------------------------------------|----------------------------------|---|---|--|--------------------------|-----------------------|
| 0 | 28.76 | 6.39 | -3.48 | -0.5744 | 5.480 | 0.395 |
| 10 | 68.75 | 12.47 | -4.99 | 2.49 | 6.343 | 0.281 |
| 20 | 93.15 | 15.12 | -5.27 | 4.576 | 5.477 | 0.294 |
| 30 | 120.39 | 17.69 | -8.27 | 1.15 | 5.507 | 0.379 |
| 40 | 151.23 | 21.95 | -10.91 | 0.13 | 6.757 | 0.358 |
| 50 | 184.17 | 17.77 | -7.60 | 2.57 | 9.695 | 0.249 |

2.2.3 Stress Path

The purpose of this paper is to carry out unloading tests to investigate the soft rock dilatancy and fracturing behavior. Thus, only the stress path and unloading rates in the tests reflect the unloading features of the excavation method and will be more meaningful.

The analytical studies [45, 46] on the stress redistribution of the surrounding rock show that the tangential stress of the surrounding rock is under a loading state, while the radial stress is under an unloading state during the underground excavation. Additionally, Eberhardt [28] explored the progressive development and evolution of excavation-induced stresses and stress paths during the advancement of the tunnel face from a three-dimensional finite-element study, as shown in Fig. 6. The excavation induced stress paths which does more apparent impact on the surrounding rock response is that the maximum principal stress (σ_1) increases and meanwhile the minimal principal stress (σ_3) decreases. Namely, the axial pressure stress increases, while the confining pressure decreases. Therefore, the stress path with reduction in the confining pressure and increase in the axial pressure stress is employed in the tests, as shown in Fig. 7.

2.2.4 Control Methods in the Tests

Stress control and deformation control are the two main control methods for triaxial tests. Generally, if the tests adopt the stress control method, the specimens may dramatically collapse when the peak stress is reached. Thus, it is impossible to obtain the post-peak stress–strain curves [15, 22]. If a deformation control mode is adopted, which is a controllable method for increasing the axial pressure and unloading the confining pressure simultaneously, complete stress–strain curves can be obtained beyond the peak strength during the excavation. Therefore, to ensure that the rock specimens can surpass the peak strength to obtain complete stress–strain curves and to reflect the actual stress

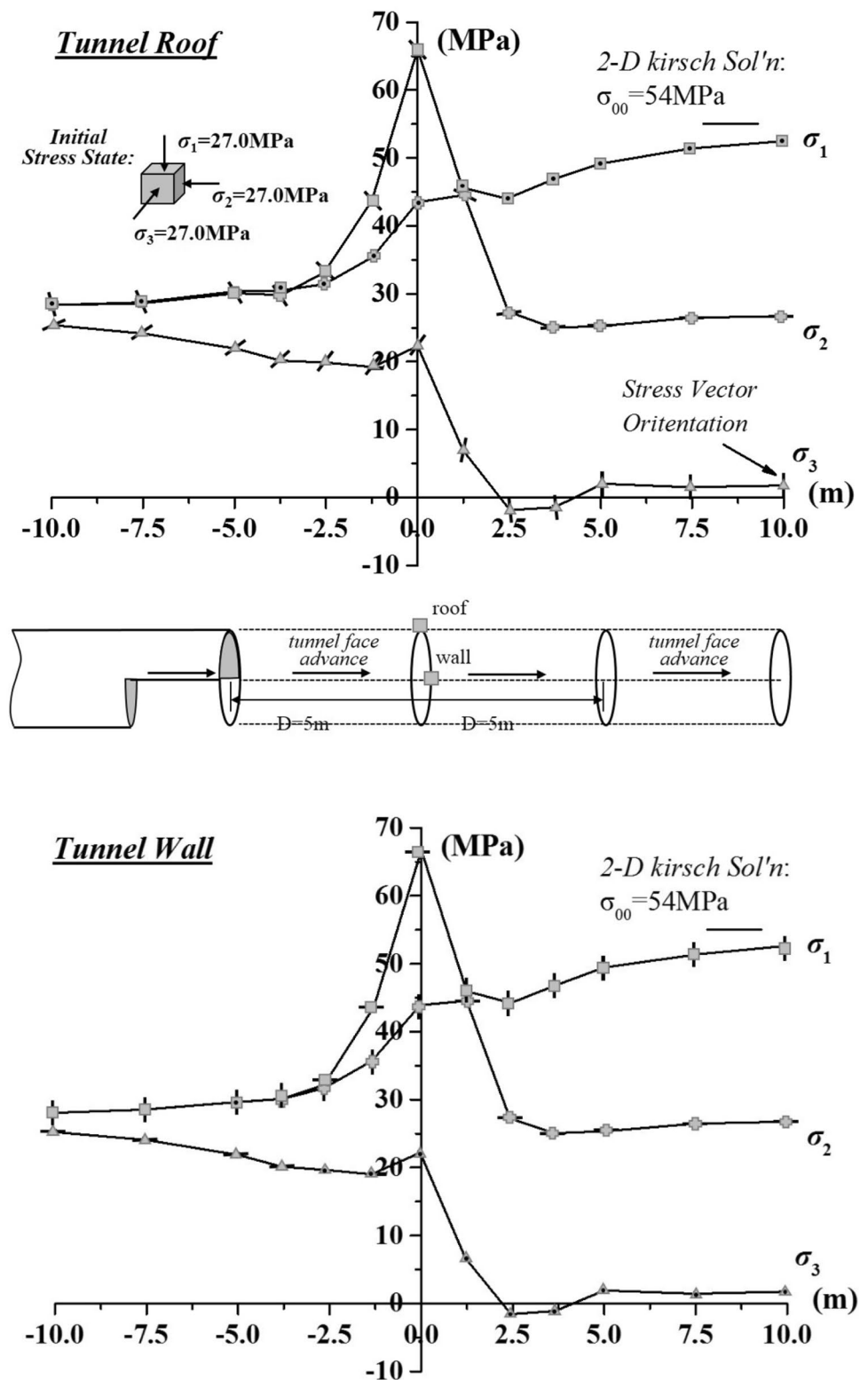
states of underground excavation, the axial deformation control mode is employed. The confining pressure and axial pressure stresses are applied during the testing process, which can recover the in situ stress state to some extent at the elastic deformation regime.

2.2.5 Unloading Rates

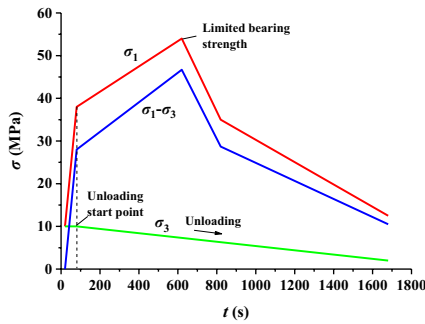
The unloading rate effects were not considered or often neglected in the previous unloading tests; however, a growing number of later studies have shown that the unloading rates have a significant impact on the rock response [47]. Some scholars have studied [47, 48] the influences of unloading rates on rock deformation and strength characteristics. But most of these studies mainly focused on hard rock, such as marble or granite and the employed unloading rates were selected mainly based on subjective experiences, which did not reflect the excavation methods especially the mechanized smooth quasi-static unloading characteristics. Therefore, further study is required on the mechanical properties of soft rock under smooth unloading rates.

The rock specimens often require time to deform and adjust. Therefore, the unloading and loading rates should not be too large. Otherwise, the obtained stress–strain curves are not accurate. Furthermore, more time is required for the tests when the unloading rates are smaller. Thus, the unloading rates cannot be too smooth. In addition, according to the excavation-induced principle stress evolution (Fig. 6) presented by Eberhardt [28], the minimum principal stress at the tunnel wall (corresponding to the confining pressure) decreases from the initial 27 MPa to approximately 1 MPa after excavation of 2.5 m. According to the tunneling records at the LXB Water Diversion Tunnel (China), the net penetration rate during TBM excavation was 2–3 m/h and the mean advance rate was about 0.8–1.2 m/s. Accordingly, it can be elementally calculated that the unloading rate is about 0.0023MP/s–0.004 MPa/s. Sometimes, the advance rate is lower than the above-mentioned rates, or the initial geostress may higher than the

Fig. 6 Stress path plots of the principal stress magnitudes and orientations at fixed points in the tunnel roof (*upper*) and wall (*lower*) for the initial stress state of hydrostatic loading (Eberhardt [28])



where σ_1 is the maximum principal stress, σ_2 is the intermediate principal stress and σ_3 is the minimum principal stress.



where, the σ_1 is the axial stress and σ_3 is the confining pressure that is applied to cylindrical specimens.

Fig. 7 Typical stress path of triaxial unloading confining pressure tests

above initial stress. Therefore, it can be estimated that the average unloading rate of mechanized excavation varies from 0.002 to 0.01 MP/s. So, according to the above calculated unloading rate, the testing experiences from previous studies [15, 47, 48] and the testing approaches suggested by the International Society for Rock Mechanics (ISRM) [44], the unloading rate in the unloading tests the confining pressure unloading rates were set as 0.005 and 0.01 MPa/s to reflect the features of smooth quasi-static unloading (mechanized tunneling). To understand the mechanical behavior under smooth unloading, a set of comparatively rapid unloading tests were also carried out, in which the confining pressure unloading rates were set to 0.05 and 0.5 MPa/s. Meanwhile, the loading speed in the axial direction was set as the axial deformation rate of 0.001 mm/s.

The above axial loading and confining pressure unloading testing procedures were controlled by a program designed in the MTS software. From the starting points of unloading, the axial stress σ_1 was increased incrementally with the axial displacement rate of 0.001 mm/s by deformation control pattern, and the confining pressure was reduced with the set unloading rates (0.005, 0.01, 0.05 and 0.5 MPa/s) until the specimen failed utterly.

2.2.6 Stresses at the Starting Points of Unloading

In other studies [49, 50], the measurement and investigation results of geostress in Huainan coal mining area have shown that the maximum horizontal principal stress is estimated to be 22–30 MPa in the rock mass along the EW direction, and the minimum principal stress is in the horizontal direction approximately 16–20 MPa. To reflect the influence of high geostress in deep ground, the initial confining pressure σ_3^0 of the unloading tests was set to 10, 20, 30, 40 and 50 MPa, respectively.

The axial stress σ_1' at the starting point of unloading should be set to be greater than the uniaxial compressive strength and approximately 60–80% of the triaxial

compression strength [15, 44]. Thus, according to the sandy mudstone triaxial compression test results (shown in Fig. 5; Table 1), the axial stresses σ_1' of the starting points in the unloading tests were set to 37, 52, 68, 82 and 102 MPa, which correspond to the confining pressures of 10, 20, 30, 40 and 50 MPa, respectively.

2.2.7 Testing Procedures

According to the deformation control method employed in the tests, the corresponding stress path and the unloading rates, the testing procedures are performed as follows:

Step 1: Apply σ_1 , σ_2 and σ_3 to the pre-set hydrostatic pressures (10, 20, 30, 40 and 50 MPa, respectively) with the loading rate of 0.5 MPa/s.

Step 2: Maintain the confining pressure σ_3 , and increase the axial stress incrementally via the stress control pattern to the unloading starting point σ_1' with a loading rate of 0.5 MPa/s.

Step 3: Increase the axial stress σ_1 continuously via the axial deformation control method with the axial displacement rate of 0.001 mm/s, and unload the confining pressure σ_3 simultaneously with the given unloading rate (0.005, 0.01, 0.05 and 0.5 MPa/s). This procedure lasts until the sample fails completely.

2.3 Dilatancy and Fracturing Properties Analyses of Soft Surrounding Rock Based on the Testing Results

The stress–strain curves from the above-mentioned unloading tests under different initial confining pressures (10, 20, 30, 40 and 50 MPa) are shown in Fig. 8. For each figure, different unloading rates (0, 0.005, 0.01, 0.05 and 0.01 MPa/s) are considered.

By comparing the stress–strain curves in Fig. 8, it is observed that the stress paths have significant influences on the deformation and failure features of the rock under loading and unloading states. Under the unloading condition, from the unloading starting point, the axial deformation curves become flattened and develop to the right. The lateral deformation acceleratingly grows. Therefore, the volumetric deformation reverses from compression to expansion. The dilatancy under unloading is more prominent than that under the loading condition when the deviatoric stresses are the same. The peak strength under unloading is obviously lower than that under loading compression. This shows that the rock under the unloading state is more prone to breaking.

A prominent phenomenon can be seen is that the shape of the stress–strain curves, the peak strength and the post-peak failure characteristics are influenced by the unloading rates greatly. In this study, this is called ‘unloading

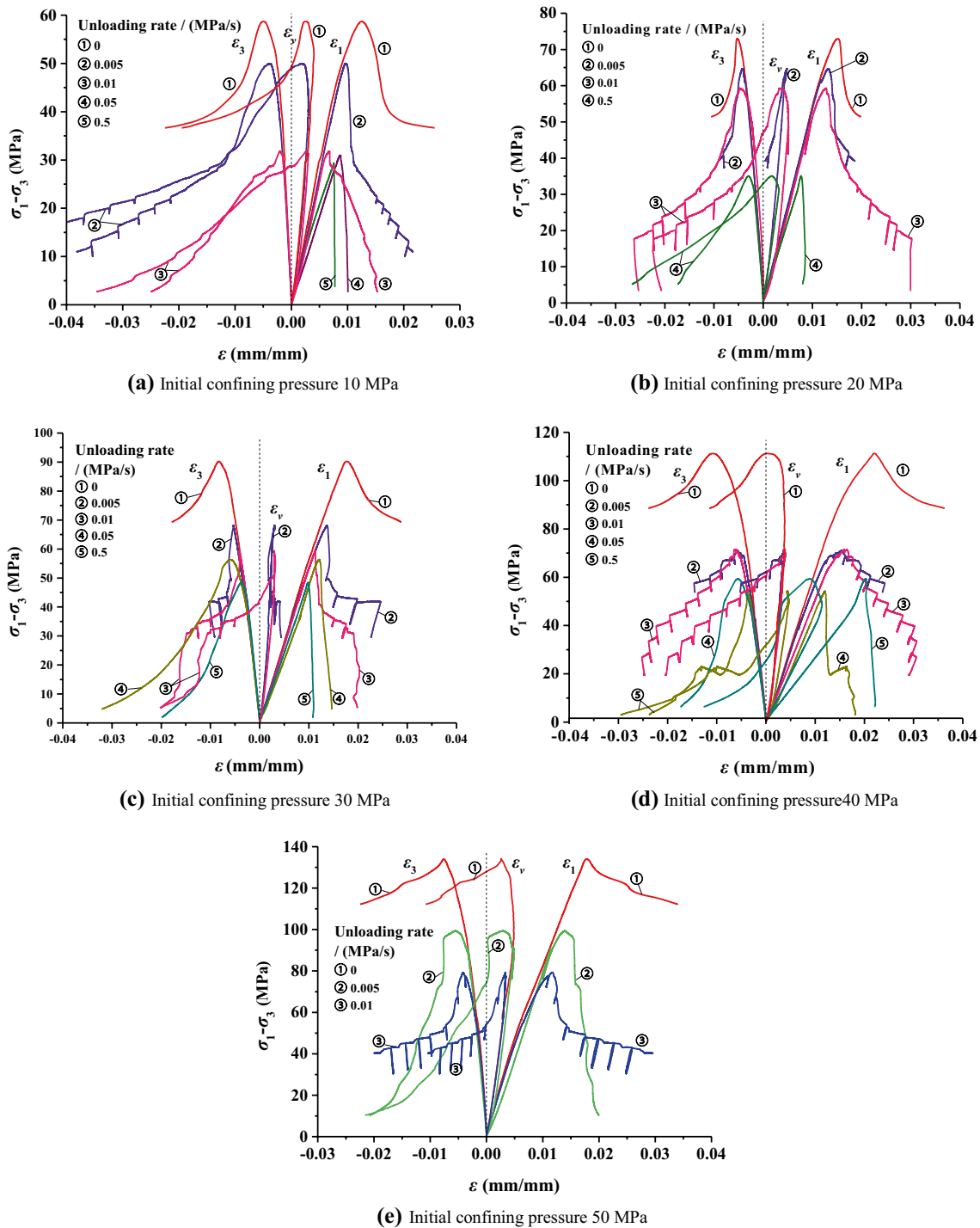


Fig. 8 Stress–strain curves of triaxial unloading confining pressure tests with different unloading rates. **a** Initial confining pressure 10 MPa, **b** Initial confining pressure 20 MPa, **c** Initial confining pressure 30 MPa, **d** Initial confining pressure 40 MPa, **e** Initial confining pressure 50 MPa

rate effects’. These effects will be analyzed in detail. In addition, the confining pressure also has similar influences. However, it will not be discussed in detail here.

2.3.1 Influence of Unloading Rate on Soft Rock Deformation Characteristics

It can be seen from Fig. 8 that under each unloading rate, the samples are under the axial loading state before

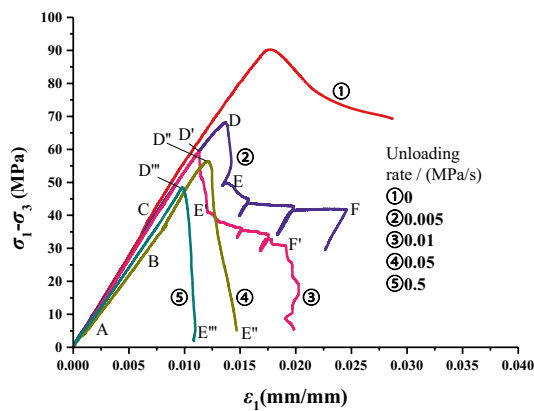


Fig. 9 Stress–axial strain curves under different unloading rates of initial confining pressure $\sigma_3^0 = 30$ MPa

unloading, and the corresponding stress–strain curves are similar to that under the triaxial compression tests. This suggests that the discreteness of the samples is small.

From the beginning of unloading, the stress–strain curves become different with the unloading rate. The axial, lateral and volumetric deformations of all the specimens [under the initial confining pressure of 10 MPa (Fig. 8a), 20 MPa (Fig. 8b), 30 MPa (Fig. 8c), 40 MPa (Fig. 8d) and 50 MPa (Fig. 8e)] are significantly affected by the unloading rates. The samples under the confining pressure of 30 MPa are taken as examples (as shown in Fig. 9) to illustrate the effect of unloading rates on the deformation and failure features. When the confining pressure unloading rate is fast, e.g., 0.05 MPa/s (Line ④ in Fig. 9) and 0.5 MPa/s (Line ⑤ in Fig. 9), the stress–strain curves at the pre-peak yield state are much different from those obtained under the triaxial compression tests. There is a sudden brittle failure approximately along the plumb line at the post-peak stage (e.g., section $D''E''$ of Line ④ and $D'''E'''$ of Line ⑤ in the stress–strain curves). However, when the unloading rate is slow, e.g., 0.005 MPa/s (Line ② in Fig. 9) and 0.01 MPa/s (Line ③ in Fig. 9), the pre-peak stress–strain curves are close to those under triaxial compression conditions. One or two brittle drops occur while beyond peak strength (e.g., section DE of Line ② and section $D'E'$ of Line ③ in Fig. 9). Then, there is linear strain softening along an oblique line with a small slope (e.g., section EF of Line ② and section $E'F'$ of Line ③), in which multistage microfractures are produced. When the speed of unloading increases, the peak strength decreases (e.g., the peak strength decreases gradually from Line ② to ③) and the amplitude and intensity of the post-peak brittle failure increase.

It is interesting that there are multistage smaller brittle drops (section FG in Fig. 9) during the post-peak linear strain softening period (phase EF in Fig. 9). The major reason is that the stiffness of MTS testing apparatus is very

high. The stresses of the sample soon recover to nearly 90% of the values prior to the brittle fall along the current brittle drop path, after which it deforms continuously in accordance with the linear strain softening law. Especially, secondary microfractures (section FG in Fig. 9) are produced due to continuous unloading at the linear strain softening stage (section EF in Fig. 9). Similar phenomenon can be seen in other samples when the unloading rate is 0.005 and 0.01 MPa/s (Fig. 8). Similar post-peak microfractures are exhibited in the stress–strain curves of marble triaxial stress relaxation tests in the studies performed by Wu [51]. However, this particular phenomenon and the corresponding reasons have not been noted explicitly. The above-mentioned feature is unique for soft rock under smooth quasi-static unloading, and it is analyzed definitely in this paper based on the testing results.

It can be seen from Fig. 8 that there are similar rules for different unloading rates under other confining pressures. Under rapid unloading (0.05 or 0.5 MPa/s), the lateral stress constraints reduce drastically, and the bearing capacity decreases sharply. When unloading is applied smoothly (0.005 or 0.01 MPa/s), the following phenomena are observed: (a) damage–dilatancy appears at the pre-peak unloading yield phase; (b) the volumetric strain curve develops toward the dilatation direction; (c) small brittle falls are produced once or twice along the penetrated fracture surface when the peak strength is first reached; (d) and linear strain softening is generated along an approximately oblique line with a small slope as the confining pressure is continuously unloaded.

The above-mentioned dilatancy and fracturing behavior (as shown in Figs. 8, 9) is closely associated with the following intrinsic reasons. When under smooth unloading, the confining constraint of the rock samples is released gently. Thus, its pre-peak stress–strain curves are close to those in the conventional triaxial compression tests. Additionally, the damage and microfractures are gradually initiated because the rock yields. The microfractures will propagate and gradually coalesce into macrofractures, then a major brittle failure occurs along the macrofractures when the stress reaches the bearing strength. Thus, the post-peak stress–strain curve behaves once or twice as brittle drops. Then, as the confining pressure continues to be unloaded with a smooth rate, the residual confining pressure is still relatively high, and the axial load is controlled by the deformation pattern. That is, the axial stress still maintains loading during the process of unloading the confining pressure. Meanwhile, the work done by the axial stress is absorbed and converted into strain energy and surface energy during unloading. Therefore, the axial loading stress plays a certain role in the fracturing process. This may promote rock damage and fracture, as well as accelerates crack extension and propagation. Thus, multistage

microfractures are observed in this phase. The deformation of rock at this stage obeys the law of linear strain softening with the decrease of confining pressure in general. When under rapid unloading, the circumferential stress constraint of the cylindrical rock specimens is removed sharply. Consequently, the bearing capacity is decreased heavily. The failure plane is formed at the firstly transient brittle failure, then the ruptured blocks slide and move along the failure-plane. So, sharply brittle drops occur when the limited bearing capacity is reached.

2.3.2 Influence of Unloading Rate on Rock Strength Characteristics

Because the experienced stress paths are different, the peak stress in the triaxial unloading confining pressure tests is different from that in uniaxial and triaxial loading tests. The confining pressure continues to decrease during the failure process, and the peak stress at the failure point reflects the limited bearing capacity of the rock during the unloading of confining pressure. To distinguish it from the concept of ‘peak strength’ in the loading test, Qiu [15] proposed a new concept of ‘limited bearing capacity’ to denote the peak axial stress level when the rock fails during the unloading confining pressure tests. Additionally, this concept is employed in this study to discuss the effect of unloading rates on the limited bearing capacity and limited strain state.

According to the test results, the changing laws of the limited bearing capacity versus the unloading rates are obtained, as shown in Fig. 10. It can be seen that: (a) the limited bearing capacity and maximum deviatoric stress are both lower than those under triaxial compression conditions, which decrease with the unloading rate generally following an exponential rule: $\sigma_{lm} = \sigma_{lm0} + Ae^{-r/t}$, and increase rapidly with the decreasing unloading rate when the unloading rate is small (e.g., 0.005, 0.01 MPa/s); (b) the

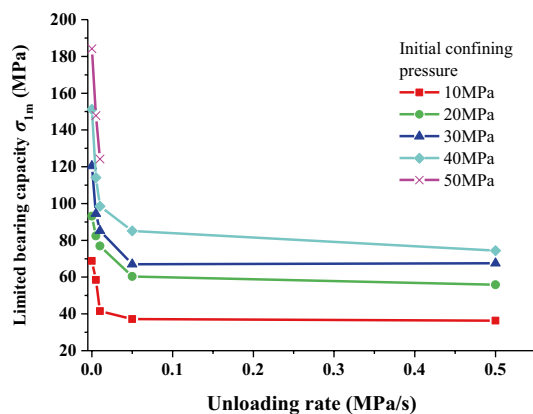


Fig. 10 Limit bearing strength and strain versus unloading rate

confining pressure unloading amount up to the rock sample failure increases with the growing unloading rate, i.e., the greater the unloading rate, the more the lateral restriction released; (c) meanwhile, when the unloading rate increases to 0.05 and 0.5 MPa/s, the confining pressure unloading amount changes a little with the unloading rates; (d) when the unloading rate decreases, the limited bearing capacity increases, and the strength parameters under the loading condition are closer to those under the triaxial compression tests.

The reasons for the above listed phenomena are that the confining restraint is still relatively high due to smooth unloading; the stress adjusts gently and uniformly at pre-peak stage; the induced microfractures interact with each other, and the frictional mechanisms of the samples are motivated; the axial pressure that needs to reach the failure point is high; and the unloaded confining pressure till the failure is small and close to the conventional triaxial compression tests. While under rapid unloading, the lateral stress constraints of the specimens are relieved dramatically, and the shear localization process was accelerated, the strength of the samples decreases greatly and the corresponding limited bearing capacity declines apparently.

2.3.3 Influence of Unloading Rate on Soft Rock Failure Characteristics

The stress paths during the unloading tests are presented in Fig. 11, and the Mohr stress circles for failure envelope analyses are plotted in Fig. 12. The stress paths and the Mohr failure circles indicate how the specimens reach the failure. They also imply that the strength of rock samples decreases with the growing unloading rate, and the samples undergo longer shearing and fracturing process at the post-peak stage when the unloading rate is smooth (0.005 MPa/s and 0.01 MPa/s).

Under the unloading state, the sample is prone to produce axial tensile cracks, and macro tensile–shear composite failure occurs. The failure differs from that under the uniaxial and triaxial compression conditions, in which a spalling failure or shear failure pattern is mainly generated.

When rapid unloading is performed (e.g., with an unloading rate of 0.05 or 0.5 MPa/s), the sample experiences a sudden brittle drop when limited bearing capacity is reached, and the experienced friction is small. The sudden brittle drop forms a single shear fracture plane that is thin and smooth, as shown in Fig. 13a, b. This is mainly because the confining restraint is released quickly, while the axial direction is still loaded under a rapid unloading situation.

As shown in Fig. 13c, d, when unloading is slow (e.g., with an unloading rate of 0.005 or 0.01 MPa/s), the unloading failure is accompanied by many axial splitting

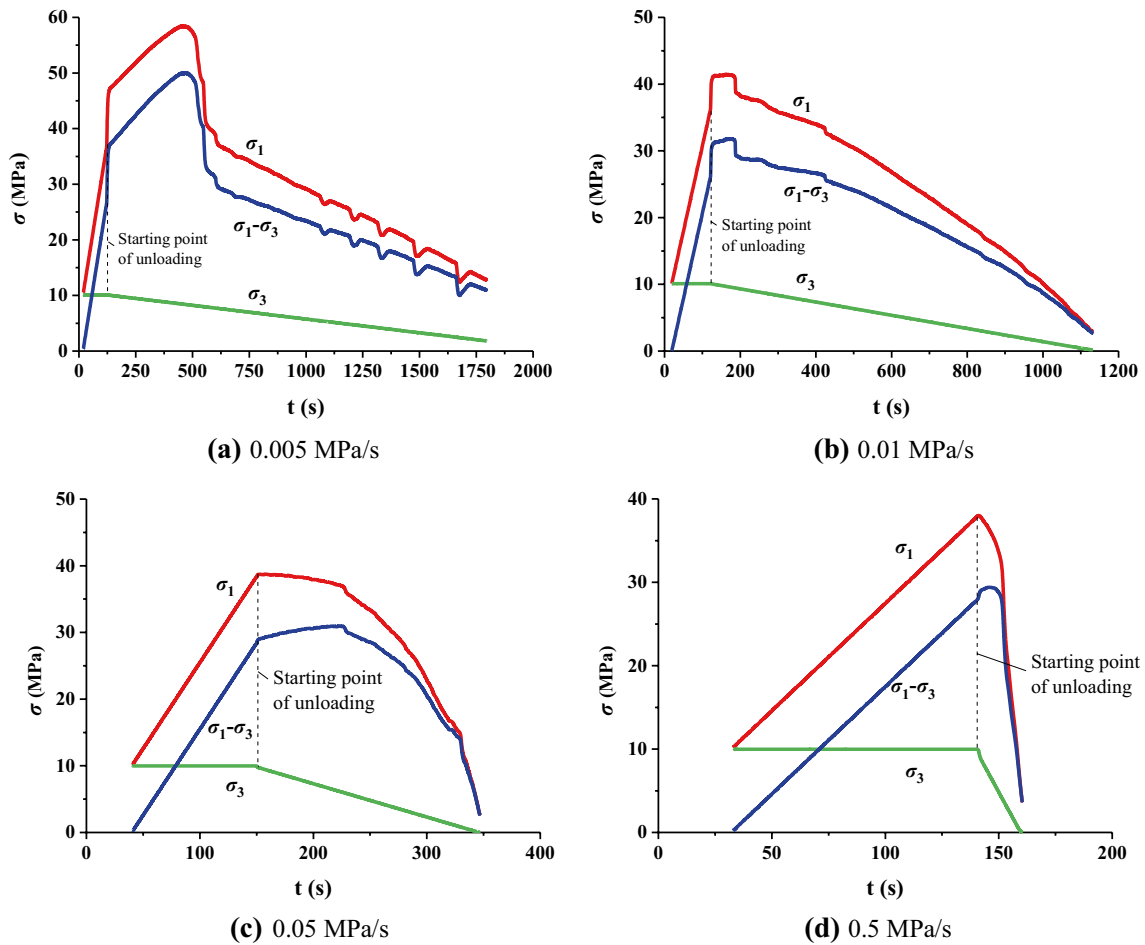


Fig. 11 Stress paths in the unloading tests with the initial confining pressure σ_3^0 of 10 MPa, a 0.005 MPa/s, b 0.01 MPa/s

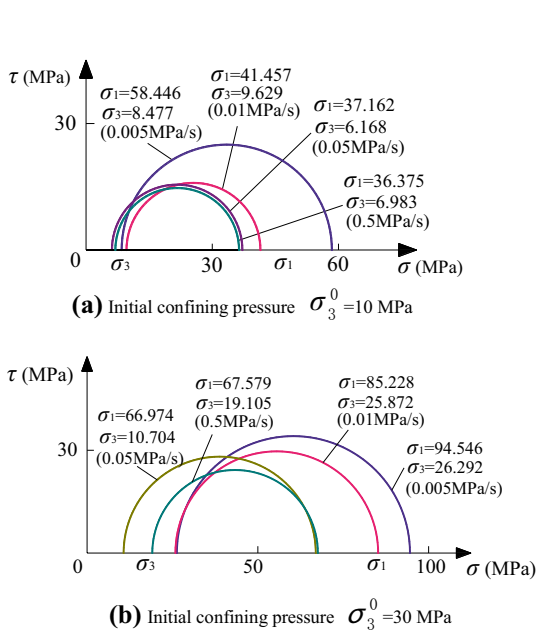


Fig. 12 Mohr's circle when the samples fail

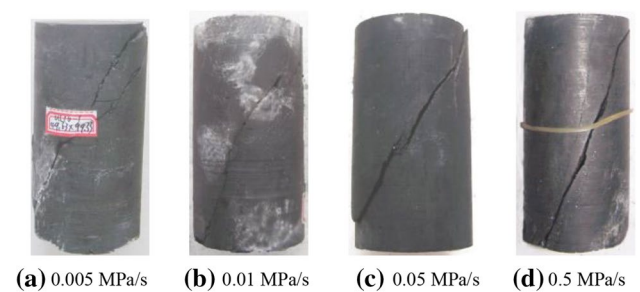


Fig. 13 Photos of the failed samples under different unloading rates (initial confining pressure $\sigma_3^0 = 10$ MPa)

cracks. The formed failure cross-plane is a shear-fragmentation band with a certain thickness, that is, because fragmentation chips and asperities will be powdered and sheared off into rock powder. Meanwhile, tiny particles are generated with the combining effects of the axial compression and shear stress along the shear fracture plane.

2.3.4 Damage Evolution Equation at the Damage–Dilatancy Stage

It can be assumed that there is only elastic deformation ϵ_1^e in the axial strain direction, and the lateral strain ϵ_3 is equal to elastic strain ϵ_3^e plus crack strain ϵ_3^c :

$$\begin{cases} \epsilon_1 = \epsilon_1^e \\ \epsilon_3 = \epsilon_3^e + \epsilon_3^c \end{cases} \quad (1)$$

where the crack strain ϵ_3^c behaves as irreversible deformation and plastic deformation.

Assuming that the main direction of damage is along the unloading direction, and it is considered that there is no damage in the axial direction, the triaxial unloading damage tensor can be expressed as:

$$D = \begin{bmatrix} 0 & & \\ & \omega & \\ & & \omega \end{bmatrix} \quad (2)$$

where ω is the damage variable.

Because the damage and dilatancy are mainly caused by the crack strain in the unloading direction, the damage variable can be represented as:

$$\omega = \frac{\partial \epsilon_3^c}{\partial \epsilon_3} = 1 - \frac{\partial \epsilon_3^e}{\partial \epsilon_3} \quad (3)$$

According to the generalized Hooke’s law:

$$\epsilon_3^e = \frac{1}{E^e} [\sigma_3 - \mu^e (\sigma_1 + \sigma_2)] \quad (4)$$

For the triaxial test, $\sigma_2 = \sigma_3$, Eq. 4 can be simplified as:

$$\epsilon_3^e = \frac{1}{E^e} [(1 - \mu^e)\sigma_3 - \mu^e \sigma_1] \quad (5)$$

Therefore, the lateral crack strain can be obtained:

$$\epsilon_3^c = \epsilon_3 - \epsilon_3^e = \epsilon_3 - \frac{1}{E^e} [(1 - \mu^e)\sigma_3 - \mu^e \sigma_1], \quad (6)$$

where E^e is the elastic modulus in the loading period.

According to the testing results, the damage variables can be calculated using Eqs. 3 and 6. The measured and fitting curves of the damage variable that changes with lateral strain ϵ_3 (the values in the diagrams represent the initial confining pressure) are shown in Fig. 14.

As seen from Fig. 14, the damage variable ω increases with the growth of lateral strain ϵ_3 , changes smoothly at the pre-peak stage and increases dramatically when the rock fails at peak strength. Its increase rate begins to reduce when the samples enter into the linear strain softening stage. When the sample is broken completely, the damage variable ω is close to 1. By fitting them, the damage evolution equations of the deformation parameters

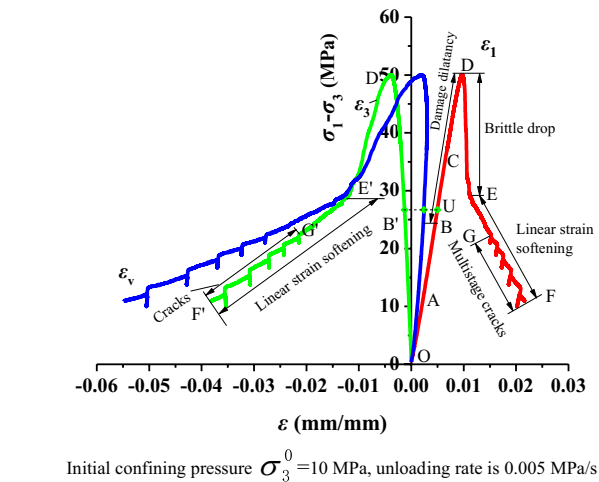
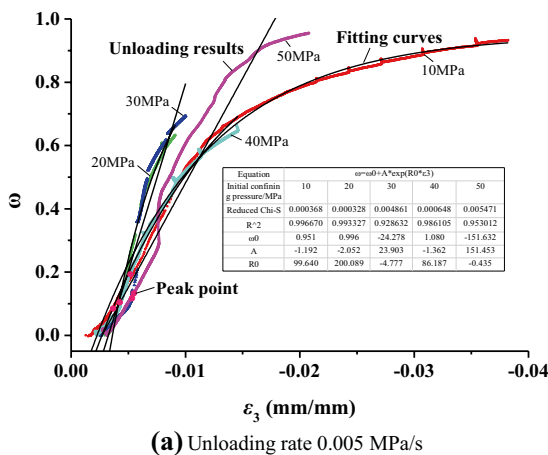


Fig. 15 Stress–strain curves under smooth unloading conditions

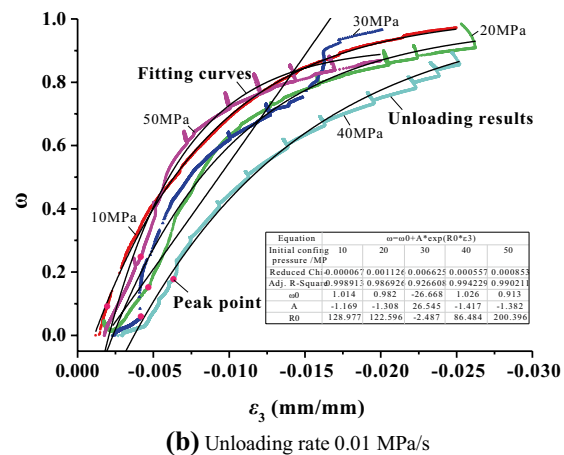


Fig. 14 The test results of the damage variable changing with lateral strain and the fitting curves under smooth unloading conditions

of sandy mudstone are obtained under the condition of smooth unloading, which obeys the exponential function $\omega = \omega_0 + Ae^{R_0\epsilon_3}$, as shown in Fig. 14.

In conclusion, when unloading rate decreases, the peak strengths and deviatoric stress–strain curves under unloading condition are close to those under the conventional loading condition. The deviatoric stress–strain curves experience the post-peak brittle drop and linear strain softening phases. When the unloading rate increases, the post-peak brittle characteristics are more apparent. Under rapid unloading (e.g., 0.05 or 0.5 MPa/s), severe post-peak brittle failure occurs. Although the residual strength regime in the stress–strain curves is not obtained in the unloading tests, the samples enter into the residual stage as long as the confining pressure unloading is stopped at the end of the linear strain softening phase. Therefore, it can be concluded that the complete deviatoric stress–strain curve of the surrounding rock under smooth quasi-static unloading is composed of an elastic deformation segment (*OB* in Fig. 15), a pre-peak unloading damage–dilatancy phase (*BD* in Fig. 15), a post-peak brittle drop stage (*DE*), a linear strain softening period that contains multistage microfractures (*EF*) and the residual strength regime.

Additionally, the unloading rate has significant influences on the rock deformation parameters (deformation modulus E and Poisson's ratio μ , compliance of strain over confining pressure $\Delta\epsilon_i$) and strength parameters (limited bearing capacity σ_{lm} , cohesion C and internal friction angle φ). The studies on these are not mentioned in detail here.

The previous study results with regard to the unloading rate effects are not much. This problem has attracted more and more attention recently. Qiu et al. [15] has studied the impacts of unloading rates on the marble deformation and failure properties, and indicates that the limited bearing capacity of marble grows with the increasing unloading rates. Zhang et al. [52] investigated the controlling influences of unloading rates on the marble mechanical behaviors too; the results showed that the rock samples' strength increased with the growth of the unloading rate. Huang et al. [48] has explored the unloading rate influences on the marble deformation, cracking and strength characteristics, and pointed out that the rock brittleness increased with the growing unloading rate. However, most of the results were based on the hard rock such as marble, and the stress paths were usually different from each other. The unloading rate effect on the soft rock under high confining pressure has been rarely studied. These previous research results are not appropriate for soft rock under smooth quasi-static unloading conditions. The employed unloading rates and stress path during the unloading tests are able to reflect the natural unloading characteristic of the excavation methods well.



Fig. 16 RLW rock triaxial rheological testing machine

3 Experimental Research on Time-Dependent Behavior of Soft Rock via Triaxial Unloading Creep Tests

The time-dependent characteristics of soft surrounding rock deformation are significant during holidays or construction standstills due to equipment maintenance or TBM stoppage, etc. [53, 54]. Therefore, laboratory creep testing is an important approach for studying the time-dependent behavior.

3.1 Test Approach

3.1.1 Testing System

Triaxial unloading creep tests were carried out using an 'RLW-500' rock triaxial rheological testing apparatus (Fig. 16) that was developed by the Institute of Rock and Soil Mechanics, Chinese Academy of Sciences and Changchun City Chaoyang Test Instrument co., LTD. The rock samples were installed as shown in Fig. 17.

The RLW system is composed of axial loading, confining pressure loading, servo controlling, data acquisition and automatic plotting systems. The load control and displacement control models can be employed and can be transformed into each other smoothly during the testing process. This experimental system is excellent for rheological testing and is suitable for performing triaxial unloading creep tests in this study.

3.1.2 Stress Path

To reflect the underground surrounding rock stress state, the creep tests adopt step-by-step unloading confining pressure approach. Meanwhile the axial loads were kept

Fig. 17 Rock sample and extensometer installation

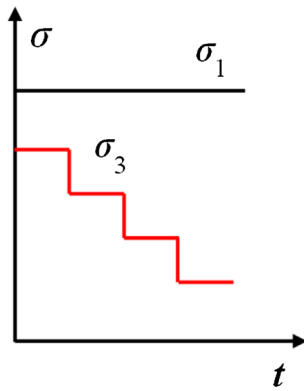


Fig. 18 Stress path during step-by-step unloading creep tests

Table 2 Deviatoric stress loading scheme of the step-by-step unloading creep test

| Sample number | UC50 | UC70 | |
|-------------------------------|-----------------|------------------------------|------------------------------|
| Initial axial compressure/MPa | 50 | 70 | |
| Stress level | σ_3 /MPa | $(\sigma_1 - \sigma_3)$ /MPa | $(\sigma_1 - \sigma_3)$ /MPa |
| The first level | 40 | 10 | 30 |
| The second level | 30 | 20 | 40 |
| The third level | 20 | 30 | 50 |
| The fourth level | 10 | 40 | 60 |

constant. Unloading was performed in four steps under four deviatoric stress levels. Refer to the incremental step loading method [44, 55]; step-by-step unloading confining pressure mode was employed in the creep tests. The unloading was performed with 10 MPa per step and the axial stress at

each stress level was constant until entering into the next creep level at a given creep time after the samples attained a stable creep state. The test terminates when unloading is completed or the sample breaks. The stress path for the step-by-step unloading creep test is shown in Fig. 18.

3.1.3 Testing Procedures

According to the triaxial compressive strength and deformation parameters of sandy mudstone shown in Fig. 5 and Table 1, the stress state under each confining pressure level of the creep test was determined, as shown in Fig. 18 and Table 2. In this study, two creep tests were carried out on two specimens (sample UC50 and UC70). The initial axial pressure was set to 50 and 70 MPa on the two specimens, respectively, and the confining pressure was unloaded from 40 to 10 MPa with a 10 MPa/step. The next step of unloading started after the previous creep reached a stable creep state. The sample UC50 maintained an axial pressure of 50 MPa, and the specimen UC70 kept an axial pressure of 70 MPa.

3.2 Creep Damage, Dilatancy and Fracturing Rules

3.2.1 Axial and Lateral Creep Rules

Through the step-by-step unloading confining pressure creep tests with constant axial loads, sandy mudstone creep laws are obtained, as shown in Fig. 19. Then, according to the experimental data processing approach for the incremental step loading creep test [44, 55], the entire curves are translated into creep curves for each stress level, as shown in Figs. 20 and 21.

As can be seen from Fig. 19~21, significant creep deformation of the sandy mudstone is produced under various stress levels, where the axial and lateral deformations consisted of unloading transient deformation and creep deformation. The creep curves include decay and steady creep characteristics. The creep deformation grows rapidly during the early stage of the creep tests under each stress level, but the creep rate soon attenuates to a steady creep rate. When deviatoric stress increases, the slopes and lasting time for attenuation creep increase, and the creep rate after reaching a steady-state creep increases. The attenuation creep often only lasts 3–15 h, but the deformation during this creep stage accounts for 60% of the total creep deformation. Thus, special attention should be given to the creep deformation in the short term after excavation. The surrounding rock during this phase is usually in the attenuation creep stage. The creep strain, which is calculated according to viscoelastic models, is smaller than the testing measured value. Thus, the creep strain of the tests contains viscoplastic deformation.

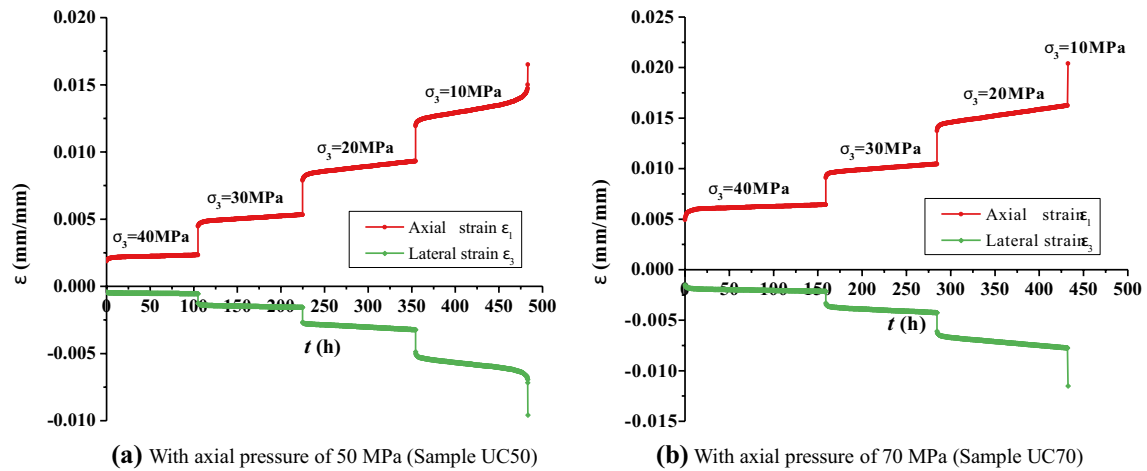


Fig. 19 Axial and lateral creep curves of sandy mudstone under different confining pressures. **a** With axial pressure of 50 MPa (Sample UC50). **b** With axial pressure of 70 MPa (Sample UC70)

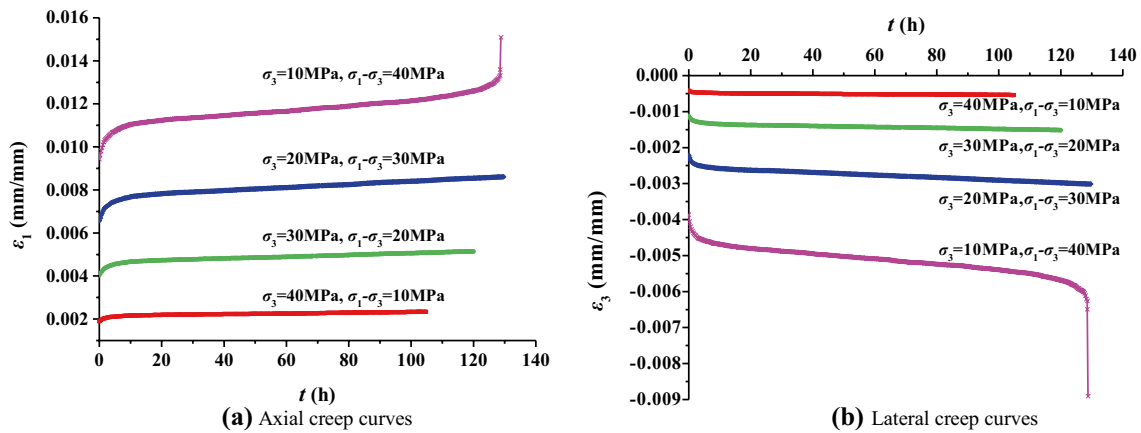


Fig. 20 Sandy mudstone unloading creep curves of the sample UC50 ($\sigma_1 = 50$ MPa). **a** Axial creep curves, **b** Lateral creep curves

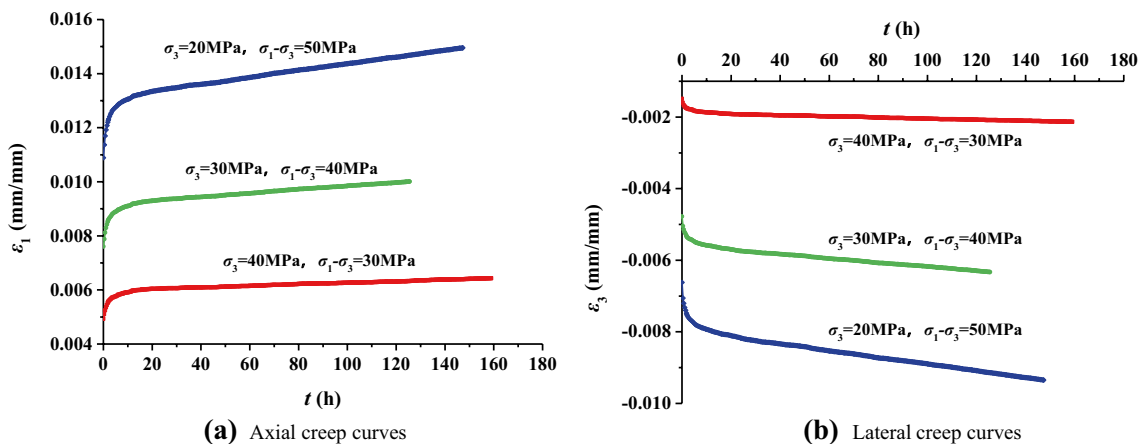


Fig. 21 Sandy mudstone unloading creep curves of sample UC70 ($\sigma_1 = 70$ MPa). **a** Axial creep curves, **b** Lateral creep curves

The lateral deformation is more obvious than the axial deformation in the unloading confining pressure rheological tests. This phenomenon is similar to the lateral dilatancy in the triaxial unloading tests; however, it is not so apparent in triaxial compressive creep tests. When the confining pressure decreases, the amplitude of the lateral creep strain increases and exceeds the axial strain. For instance, when the confining pressure of sample UC50 is unloaded from 40 to 30 MPa, its lateral creep deformation increases by 218%, and the axial creep deformation grows by 148%. Thus, the increased amplitude of the lateral rheology deformation is much greater than the axial deformation. Under the failure confining pressure level, lateral expansion is more likely to occur. The lateral strain is lower than the axial deformation, but the ratio of lateral creep deformation to lateral instantaneous deformation is greater than the axial deformation under each confining pressure level. For example, when the confining pressure of sample UC50 is unloaded from 40 to 10 MPa, the ratios of lateral creep strain to instantaneous strain are 29.710, 35.326, 35.894 and 35.326%, respectively, which are larger than the ratios (23.764, 27.581, 31.023, 60.097% respectively) of axial creep strain to instantaneous strain under the same stress level. Sample C70 follows the same rule.

3.2.2 Volumetric Creep Rule

According to the sandy mudstone unloading creep testing results (Fig. 19), the laws of volumetric strain curves changing with time for samples UC50 and UC70 under various load levels were obtained (as shown in Fig. 22).

Figure 22 shows that the changing laws of volumetric strain are more complicated than the creep rules of axial and lateral strain. The first and second stress levels of UC50 are relatively low compared with the rock yield strength, and overall it is in a volumetric-compression state.

When unloading to the third stress level ($\sigma_1 - \sigma_3 = 30$ MPa), the variety of creep volumetric deformation is small at this creep stage and remains nearly stable. Once the stress state is at the fourth stress level (when the confining pressure is unloaded to 10 MPa), the microcracks propagate and connect together and secondary cracks are initiated. The lateral strain of the specimens grows faster than the axial strain. Consequently, the volumetric strain deviates to the dilatancy direction obviously and dilates continuously with time during the creep process (an obvious creep–dilatancy). When the specimen enters into the accelerating creep stage, its volume accelerates until the specimen fails. It can be seen that the volumetric strain of the sample with an axial pressure of 50 MPa (UC50) experiences an evolutionary process from volumetric compression to constant volume and finally reaches dilatancy during the creep. Because the deviatoric stress level of specimen UC70 is higher than the yield strength since the first level loads, its volumetric strain deviates to the dilatancy direction under the first stress level in the creep process. The volumetric strain deviates to the dilatancy direction with a rapid rate when its confining pressure is unloaded to the second stress level, and the volume of the sample begins to expand.

The above-mentioned volumetric strain evolution law during the unloading creep process shows that the bearing capacity of the sample degrades with decreasing confining pressure and increasing creep time. The volumetric expansion during the creep process is mainly due to the internal microcrack propagation and secondary fracturing, which results in irreversible deformation or even final breakage.

3.2.3 Deviatoric Stress–Strain Relationships During the Unloading Creep Procedure

The deviatoric stress–strain curves of sandy mudstone are obtained to further study the mechanical behavior in

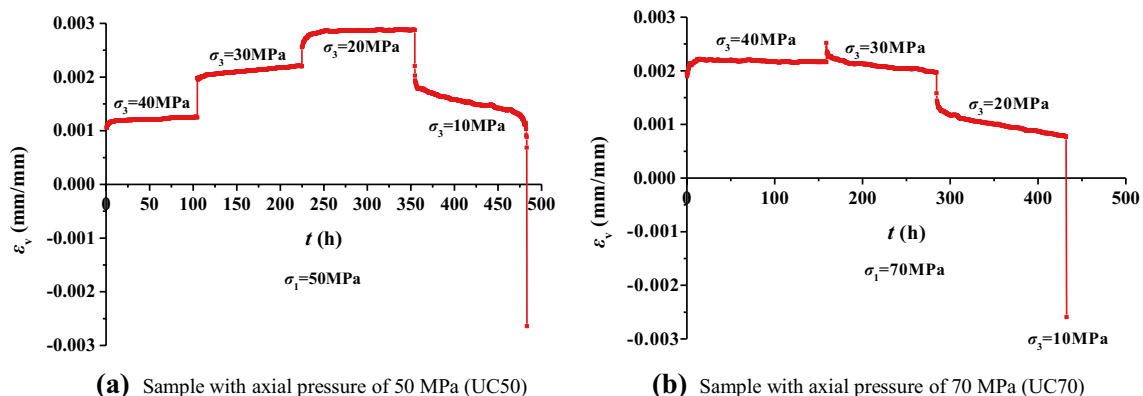
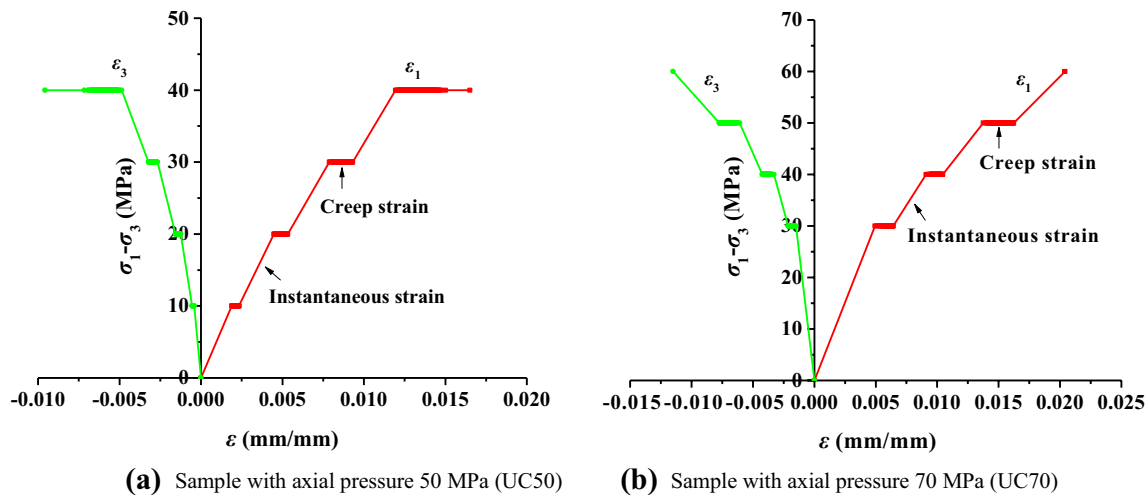


Fig. 22 Volumetric strain curve of sandy mudstone versus time under different confining pressures. **a** Sample with axial pressure of 50 MPa (UC50), **b** sample with axial pressure of 70 MPa (UC70)



The line parallel to the horizontal axis is creep strain, and the oblique line is instantaneous strain for unloading confining pressure

Fig. 23 Deviatoric stress–strain curve of sandy mudstone during the process of unloading rheology

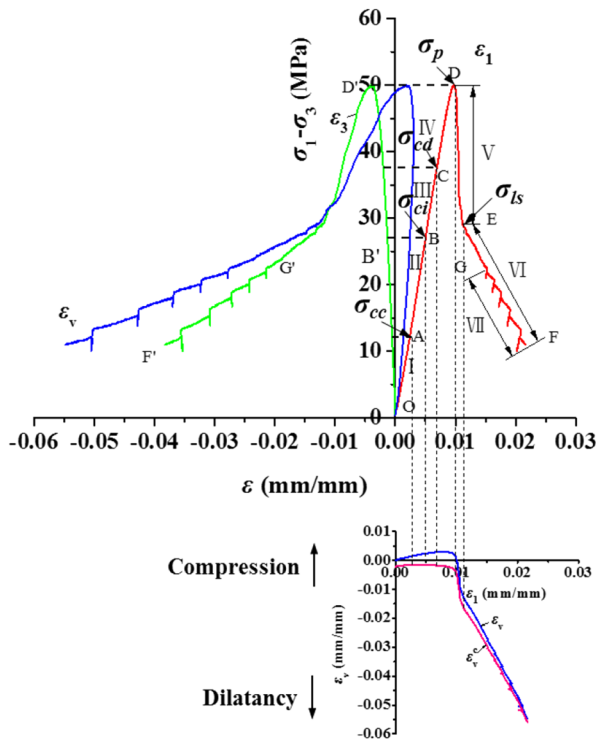
the unloading creep process, as shown in Fig. 23. It can be seen that the instantaneous deformation at the unloading instant changes obviously. The axial strain curve slope of specimen UC50 decreases from 5.303 GPa on the first creep stage to 3.819 GPa on the fourth stage, and the lateral strain curve gradient decreases from 23.904 GPa on the first stage to 6.079 GPa on the fourth stage. The axial strain curve slope of specimen UC70 decreases from 6.078 GPa in the first stage to 3.042 GPa in the third stage, and the lateral strain curve gradient decreases from 20.140 GPa in the first stage to 5.441 GPa in the fourth stage. This indicates that, with the decrease of the confining pressure and the growing creep time, the slopes of the axial and lateral deformation curves gradually decrease, and the slopes of the lateral deformation curves decrease more intensely with a greater amplitude. That is to say, the lateral expansion rate is greater than the axial compression rate.

The reasons for the above time-dependent dilatancy and fracture evolution process are mainly the relieving of the lateral restraint and damage accumulation during the creep process. When under a initial high confining pressure and low deviatoric stress level, the sample is relatively integrated and its accumulated damage is small. Thus, the instantaneous deformation and creep deformation are both small, and the ratio of the creep to the instantaneous deformation is also small. However under the first stress level, the stress does not reach the sample's yield strength. Thus, the transient deformation is mainly elastic, and a certain amount of damage occurs during the creep process. When entering the subsequent stress levels, its instantaneous deformation includes both elastic and plastic deformation, which is affected by the creep damage produced at the previous steps. Further damage is generated at this creep stage,

which aggravates this creep phase. With decreasing confining pressure, the deviatoric stress and plastic deformation increases, and vertical tensile cracks are initiated within the rock samples and expand gradually, resulting in obvious lateral expansion at the instant of unloading. The propagation of microcracks is accelerated with the creep time. Additionally, the damage is accumulated with the creep time and the confining pressure unloading amount until eventually to failure. With continual unloading, during low confining pressure and high deviatoric stress, accelerated creep occurs and the damage is accumulated to the failure limit, and finally the macro main fractures are formed. This evolution process is accompanied by an obvious lateral expansion during the creep (Fig. 22), which is similar to the lateral dilatancy in the triaxial unloading tests. It can be seen from the surface of the sample and internal cracks that some vertical extensional cracks are produced on the rock surface, and the cracks develop internally at the same time. In summary, the mechanism of time-dependent deformation of soft rock (e.g., sandy mudstone) over a relatively long term after tunneling is as follows: creep damage, time-dependent extension and development of microcracks, which is called 'time-dependent damage and fracturing' in this study.

4 Deformation Mechanism of Soft Rock

Based on the above dilatancy and fracturing results, the deformation mechanism can be discussed at the excavation instant and considering the 'time' factor in a certain time after excavation, respectively.



Initial confining pressure $\sigma_3^0 = 10$ MPa, unloading rate is 0.005 MPa/s

Fig. 24 Typical deviatoric stress–strain curve of sandy mudstone under smooth unloading conditions

4.1 Deformation Mechanism at the Excavation Instant

The inherent reasons for rock deformation and failure are the internal stress adjustment and the interior structure evolution. In damage mechanics [56], it is believed that rock damage is closely related to microcracking activities, and the yield and failure of the rock are the macro results of microfracture development and cracking.

The intrinsic fact of soft rock squeezing and large deformation is volumetric dilatancy. Therefore, to reveal the deformation mechanism of soft rock, the evolution rules of rock volumetric strain along with internal structure changes in the progressive failure process must be studied in detail.

This study uses plastic volumetric strain to represent the crack volumetric strain. According to the unloading test results in Sect. 3, the typical deviatoric stress–strain curve and the plastic volumetric strain of sandy mudstone in the unloading confining pressure process are shown in Fig. 24. The stress–strain curves and the progression of volumetric dilatancy and fracturing can be divided into the following four stages, and the intrinsic mechanisms are analyzed.

(1) Volume compression stage (Phase I in Fig. 24—segment OA).

Because of the closure of the initial pores, initial joints and microcracks within the rock, the axial compressive strain is greater than the lateral strain in this regime. Therefore, volume compression appears.

(2) Elastic stage (Phase II in Fig. 24—segment AB).

In this phase, the volumetric strain decreases with the stress linearly. The stress–strain relationship and volumetric strain generally obey a linear relationship. The starting point of this phase is called crack closure stress σ_{cc} .

(3) Pre-peak dilatancy stage, which can be subdivided into Stages III and IV.

① Phase III—segment BC in Fig. 24.

When the deviatoric stress continues to increase, the cracks begin to develop and extend. Consequently, the volumetric strain curve starts to deviate from the original straight line and turn to the expansion direction, which indicates that the volume changes from compression to dilatancy.

There are two important stress characteristic points at this stage: initial dilatancy stress σ_{ci} (Point B in Fig. 24) and damage–dilatancy stress σ_{cd} (Point C in Fig. 24). Previous studies have shown that when the stress exceeds the initial dilatancy stress σ_{ci} , the native cracks develop and propagate mainly along the pores or boundaries among the mineral particles and then randomly form new cracks. However, the length of the cracks generated at this stage is not larger than the scale of the particle size. In addition, due to the microcrack extension and propagation, the stress concentration of the crack tips tends to be alleviated, and the energy released by the crack extension is absorbed by new fracture surfaces. Further propagation of cracks requires the stress to be increased continuously. Thus, it behaves as a steady crack extension during this stage.

When the cracks extend steadily to a certain degree, the rock enters into a critical state such that the newly formed crack surfaces cannot absorb the entire energy released by crack extension. Thus, the cracks acceleratingly extend from stable to unstable propagation. Then the rock enters into the fourth deformation stage (Stage IV). The corresponding onset stress of this critical state is called damage–dilatancy stress σ_{cd} .

② Phase IV—segment CD in Fig. 24.

Phase IV starts from the damage–dilatancy stress σ_{cd} . Then, the rock begins to enter into the yield stage. This stress point corresponds to the maximum volumetric compression and is the inflection point of the volumetric–axial strain curve.

During this stage, the rock fractures propagate, intersect and coalesce as the stress continues to increase, and potential failure surfaces tend to form gradually. When the stress reaches the peak strength, the cracks may connect and penetrate into macroscopic fractures. Generally, the

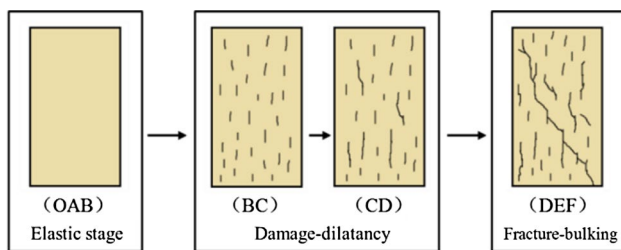


Fig. 25 Damage–dilatancy and fracture–bulking evolution processes under unloading conditions

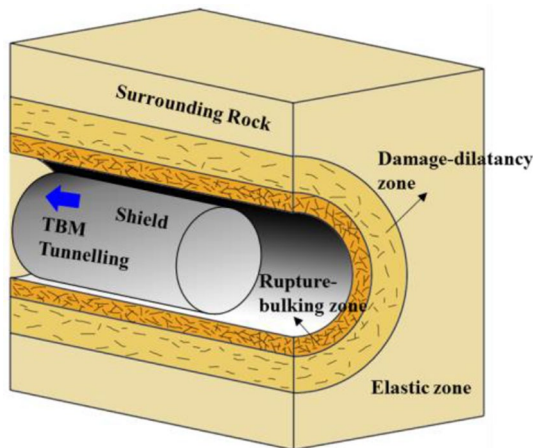


Fig. 26 Excavation damage zone of the surrounding rock during TBM tunneling

cracks propagate unstably at this pre-peak damage–dilatancy stage.

(4) Post-peak fracturing stage, which is also subdivided into Stages V and VI.

① Phase V—segment *DE* in Fig. 24.

The post-peak stage starts from the peak stress σ_p . The cracks propagate into macroscopic fracture surfaces at the peak stress point. This indicates that brittle drop occurs immediately along a vertical line, which is accompanied by the steep reduction of bearing capacity reducing. That is to say, the ruptured blocks will slide and rotate along the firstly generated fracture surfaces. Furthermore, because the confining pressure is unloaded smoothly, the confining pressure unloading amount is small when brittle drop takes place. Therefore, the residual confining pressure is relatively high, which will prevent sliding and rotation to a certain extent after failure. This phase is called the brittle drop stage.

② Phase VI—segment *EF* in Fig. 24.

This phase is called linear strain softening stage. The starting point stress of this stage is called linear strain softening starting stress σ_{ls} . Because the confining pressure is unloaded slowly, the residual confining pressure

is relatively high, which can largely prevent sliding and rotation after failure. As the confining pressure continues to be unloaded, the rock bearing capacity further declines and results in multiple secondary fractures, which is characterized by the secondary brittle drops appearing in the stress–strain curve and the rock continuing to deform following the linear softening rule. With the increase of damage and fractures within the sample, the cracks' extension and penetration are enhanced and intensified, and the scale of the secondary fractures increases greatly. Therefore, under the condition of smooth unloading, multistage secondary fractures are produced, forming a shear-fragmentation band with a certain width. The volume at this stage acceleratingly increases.

In conclusion, according to the above analyses of the dilatancy and fracturing behavior under the smooth quasi-static unloading condition, the soft rock deformation and failure process under smooth unloading confining pressure with a high initial value can be summarized as a damage–dilatancy and fracture–bulking process, as shown in Figs. 25 and 26. Pre-peak damage–dilatancy mainly denotes the initiation and propagation of microcracks until the stress reaches the peak strength. While beyond the peak strength, the microcracks coalesce and connect together, forming macrofracture surfaces. The ruptured blocks slide and dislocate along the firstly formed fracture surfaces. Then, with continuous unloading, multistage secondary cracks are initiated. With these cracks mutually penetrating, the fractured blocks further rotate, slide and flip, resulting in remarkable volumetric expansion. Thus, the post-peak fracture–bulking deformation accounts for the maximum part of squeezing and large deformation.

4.2 Deformation Mechanism Considering Time-Dependent Effect

Due to the smooth unloading rate and gentle stress adjustment, the disturbed zone and convergence both are comparatively small at the excavation instant. Another significant feature of soft rock is that its time-dependent effect is significant and its convergence speed is slow. An obvious time-dependent convergence may often arise during construction of the standstill or supports' installation.

The time-dependent deformation of surrounding rock is mainly caused by the following two parts:

1. The first is that the cracks and fractures produced at the excavation transient further develop, slip, rotate and flip with time.
2. Second, the initial damage of the surrounding rock near the tunnel perimeter is produced after stress redistribution at the excavation unloading transient. The damage within the rock is accumulated with time, thus

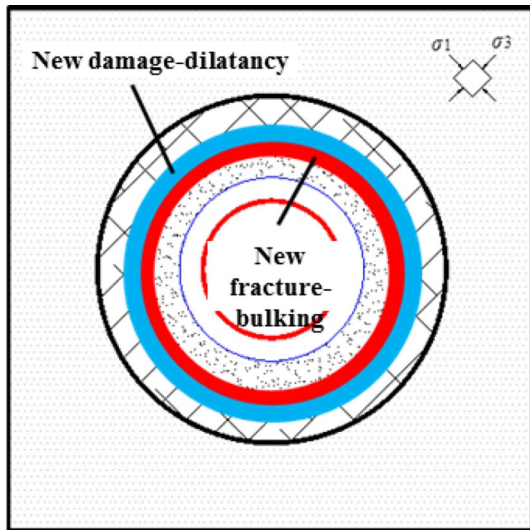


Fig. 27 Excavation damage zone at the stoppage time after TBM tunneling (*t*)

the bearing capacity degrades. New microcracks and fractures are initiated and propagate time-dependently and are accompanied by significant lateral expansion during the creep. This causes one part of the pre-peak unbroken blocks at the excavation unloading transient to reach the peak strength and then enter into the post-peak fracture–bulking state, while the other part remains within the pre-peak zone and deforms continuously. Meanwhile, the post-peak ruptured blocks in the fracture–bulking stage at the excavation instant are squeezed and produce further movement (dislocation, slippage, rotation), or even further fail due to the newly generated deformation and fractures of other original pre-peak damage–dilatancy blocks, as shown in Fig. 27. The above-mentioned process is called ‘time-dependent damage and fracture’ in this paper.

This indicates that in deep soft ground, the deformation and failure will be more serious during the tunneling stoppage time, which will be more likely to induce

hazards such as supports overloading or shield jamming in TBM tunneling.

In conclusion, the deformation of soft rock after excavation unloading is mainly composed of two parts: (1) pre-peak damage–dilatancy and post-peak fracture–bulking at the excavation unloading instant; (2) creep–dilatancy caused by the time-dependent damage and fracturing.

The above revealed damage, dilatancy and fracturing evolution processes are in agreement with the previous laboratory studies in literature and field monitoring results, which will be discussed in the following section.

5 Discussions

5.1 Laboratory Tests on the Deformation and Failure Properties of Soft Rock

The deformation mechanism of soft ground during tunneling has been revealed in the above analyses through the triaxial unloading confining pressure tests and unloading creep tests. The complete deformation and failure process from the excavation instant to the relatively long-term situation is essentially the damage and crack development and evolution, which behaves as pre-peak damage–dilatancy, post-peak fracture–bulking and its evolution with time macroscopically.

Particularly, the stress paths of the unloading tests reflect the stress state after excavation, and the unloading rates represent the unloading characteristics of the tunneling methods. This paper primarily focuses on the quasi-static mechanized tunneling method, and the time-dependent behavior of soft rock is emphasized and attracts significant attention, which is of great importance for understanding the actual deformation mechanism of soft rock.

However, the experimental investigation in this paper mainly focuses on the volumetric dilatation in terms of damage evolution and fracturing behavior during the excavation unloading and creep process, but mostly on a macroscopic scale. The soft surrounding ground experiences crack initiation and fracture network propagation, after which the ruptured blocks are generated and produce further movements. The movements include dislocation and

Fig. 28 The convergence and fracturing monitoring stations

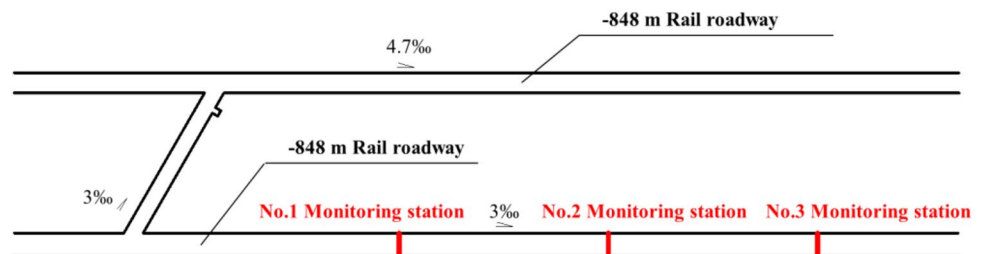




Fig. 29 The surrounding rocks are fractured and dilatant, finally producing heavy squeezing deformation

rotation among the ruptured blocks, which means that discontinuous deformation is generated. Thus, it should be noted that the crack initiation and fracture network propagation need to be paid sufficient attention. The corresponding laboratory tests and theoretical criteria to be carried out will contribute to understanding the squeezing and large deformation of soft rock.

Many researchers have performed the experimental studies on the damage, dilatancy and cracking evolution. For example, Qiu et al. [15] carried out an incrementally cyclic loading–unloading pressure test to quantify stress-induced damage and fracturing under the condition of triaxial unloading confining pressure. The results demonstrated that the rock underwent the evolutionary process of pre-peak unloading damage and volumetric dilation as well as the fracturing behavior. Chen et al. [26] had performed

triaxial unloading confining pressure tests to determine the dilatancy and creep characteristics under unloading confining pressure. The results implied that the volume deformation of rock salt under unloading was more than that under triaxial loading, and the corresponding dilatancy rate decreased as the confining compression increased under the same axial compression; the associated creep rate depends on the deviatoric stress and confining compression values at the end of the unloading process. Wang et al. [36] performed experimental investigations for the creep–damage–rupture behavior of rock salt. The testing results also indicated that the rock underwent instantaneous creep–damage, dilatancy, cracking, rupture and finally long-term failure. The revealed damage, dilatancy and fracture evolution processes in this paper coincide with the previous laboratory studies in the literature. Furthermore, this study takes the unloading rates and unloading stress path into consideration, which reflected the unloading characteristics of the excavation methods. In addition, the time-dependent dilatancy and fracturing behavior are considered in the study for soft rock response. So the investigation results, in which both the transient and temporal response are studied, are able to capture the actual damage, deformation and failure behavior of soft rock under the excavation unloading effect and more accurate stress redistribution.

5.2 Constitutive Models and Numerical Modelling Methods for Soft Rock

Deformation calculation and prediction is most important for soft rock deformation analyses. Many previous studies [2, 11] have focused on employing some qualitative, semi-quantitative and quantitative deformation or stress indexes to predict and evaluate the soft rock deformation potential. However, the current analytical solutions and numerical

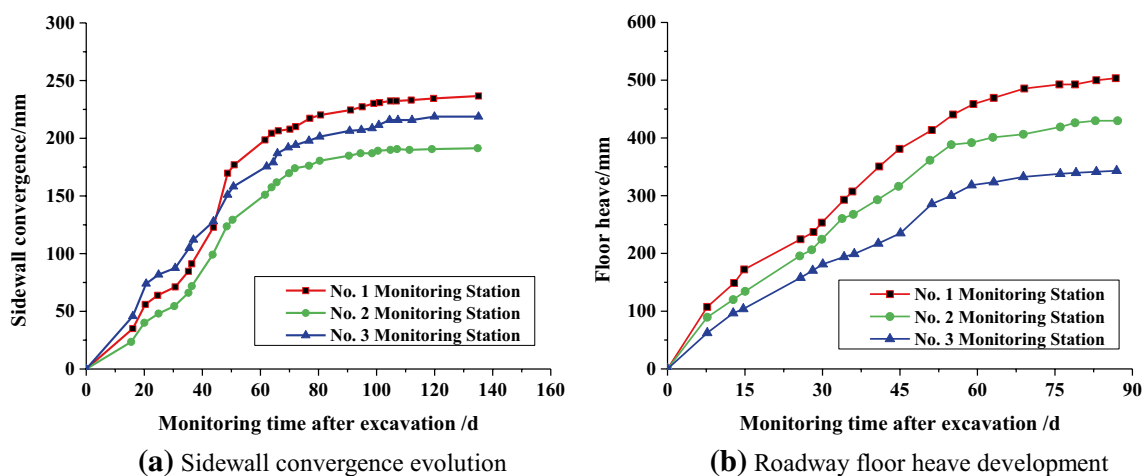


Fig. 30 Convergence monitoring results. **a** Sidewall convergence evolution, **b** roadway floor heave development



Fig. 31 Microfractures evolved into macrocracks or even big fissures on the roadway floor

simulation methods are still not capable of capturing the soft rock dilatancy and fracturing behavior accurately.

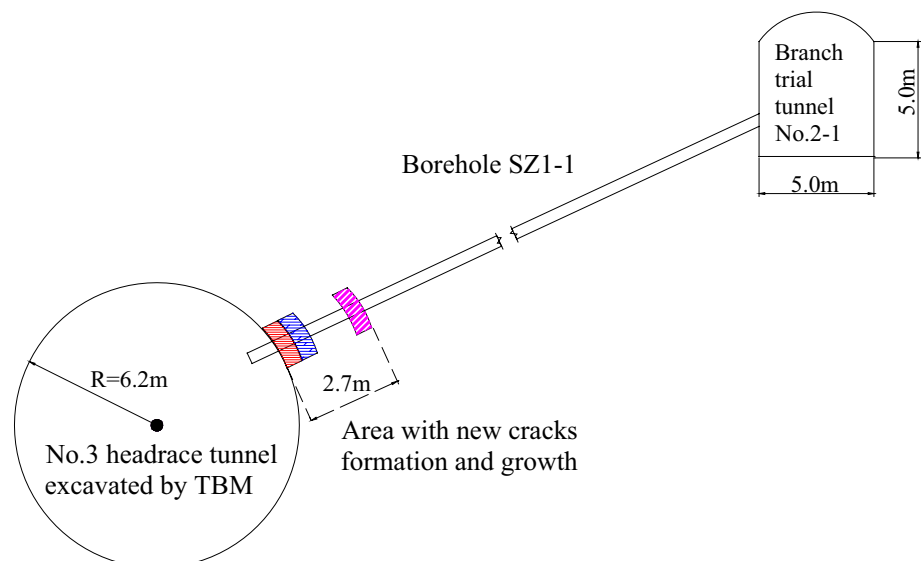
Thus, another important issue is to establish accurate constitutive models and put forward suitable numerical methods to model the soft rock dilatancy and fracture behavior. However, the constitutive models and numerical methods need to be set up based on the deformation mechanism rigorously. The above revealed mechanism shows that the soft rock deformation consists of pre-peak damage–dilatancy, post-peak fracture–bulking and creep–dilatancy. That is to say, the soft rock deformation, especially squeezing and large deformation, is composed of both continuous and discontinuous deformation. Therefore, the continuous–discontinuous models need to be established to

describe the dilatancy and fracturing procedure. Additionally, the significant viscosity should be taken into account. For example, the time-dependent behavior and its corresponding creep models (CVISC and VIPLA model) for soft rock deformation have been studied by Bonini [57]; Sterpi and Giada [58] proposed an elasto-viscoplastic rheological model; Debernardi and Barla [35, 53] put forward a new stress hardening elasto-viscoplastic constitutive model (SHELVIP model) to describe the soft rock squeezing behavior. Besides, numerical simulation is an effective approach for studying the rock deformation and failure procedure (Hasanpour et al. [59]; Zhao [60, 61]). The experimental results presented in this study provide a basis for further research regarding the constitutive model establishment of soft rock during excavation. However, most of the current numerical methods cannot reflect the above-mentioned continuous–discontinuous deformation and failure procedure of soft rock essentially. The numerical modeling method based on the continuous–discontinuous coupling analyses methods such as FDEM (combined finite-discrete element method) [62] and NMM (numerical manifold method) [63] may be feasible and suitable ways for modelling the squeezing and large deformation of soft rock, which is currently our main research focus.

5.3 In Situ Monitoring of Soft Rock Deformation Processes and Validation of the Revealed Mechanism

Another effective means for investigating soft rock deformation mechanism is in situ monitoring. Additionally, the field measured data can further predict surrounding rock convergence and validate its corresponding mechanism. Currently, in situ monitoring methodologies include

Fig. 32 Schematic drawing of new crack location based on digital images analysis of the test borehole SZ1-1 [65]



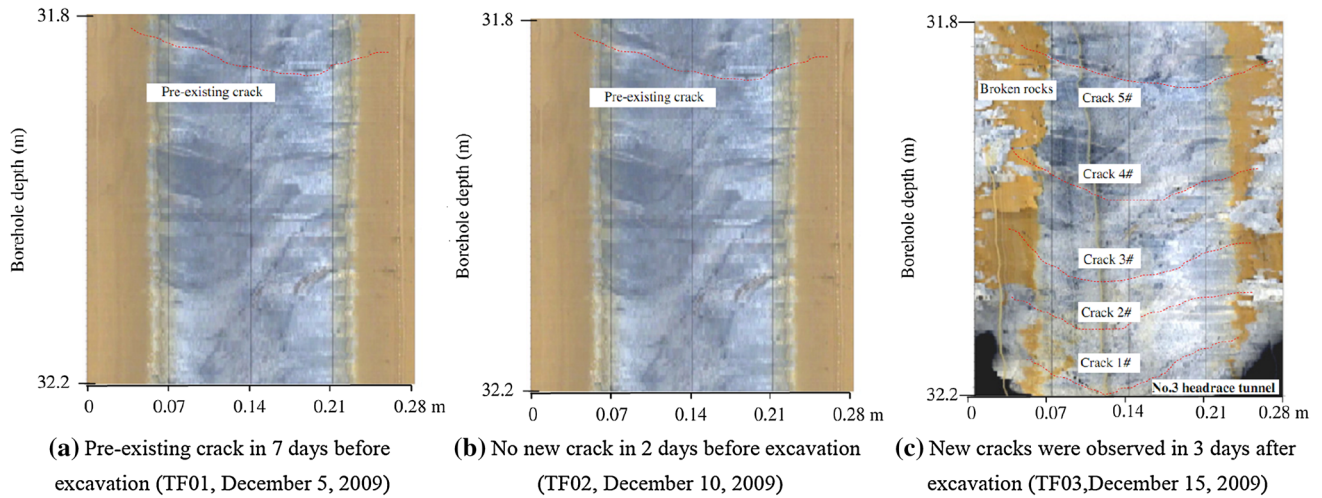
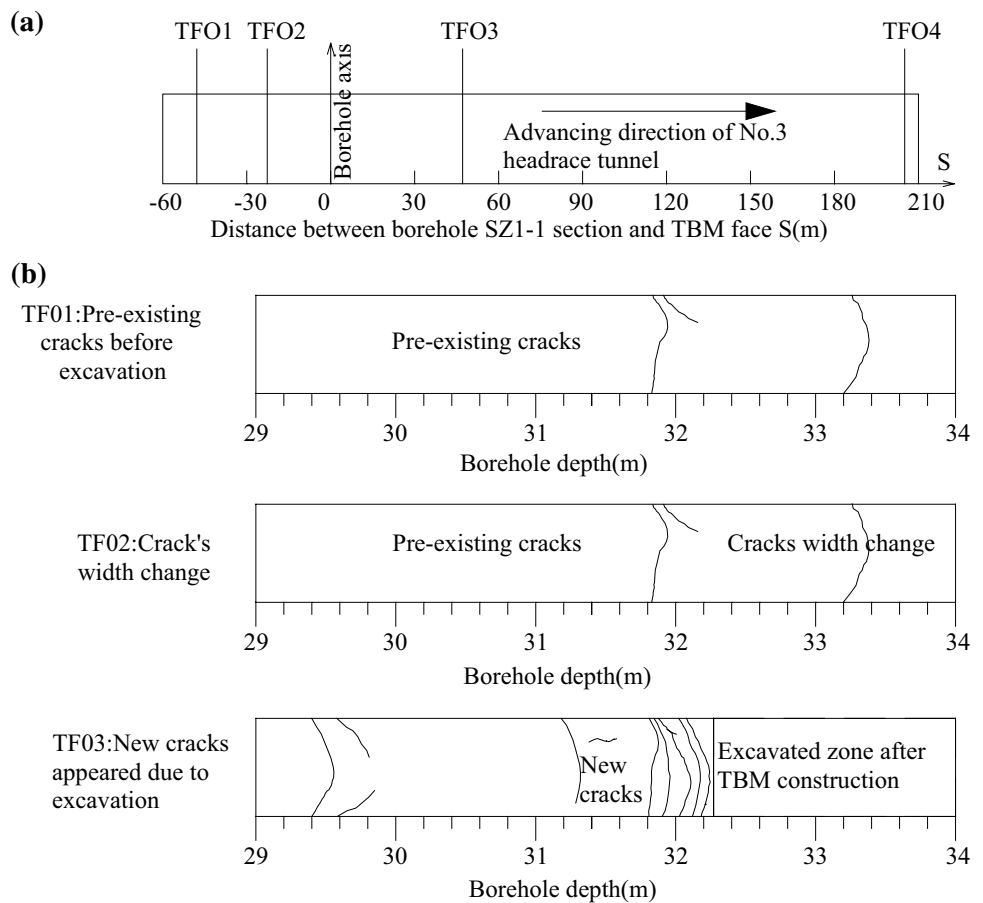


Fig. 33 Borehole images of fracture initiation and evolution in EDZ at the borehole depth of 31.8–32.2 m during different excavation stages monitored in head race tunnel No. 3 at Jinping II hydropower station (China) [64, 65]. **a** Pre-existing crack in 7 days before excavation (TF01, December 5, 2009)

b no new crack in 2 days before excavation (TF02, December 10, 2009), **c** new cracks were observed in 3 days after excavation (TF03, December 15, 2009)

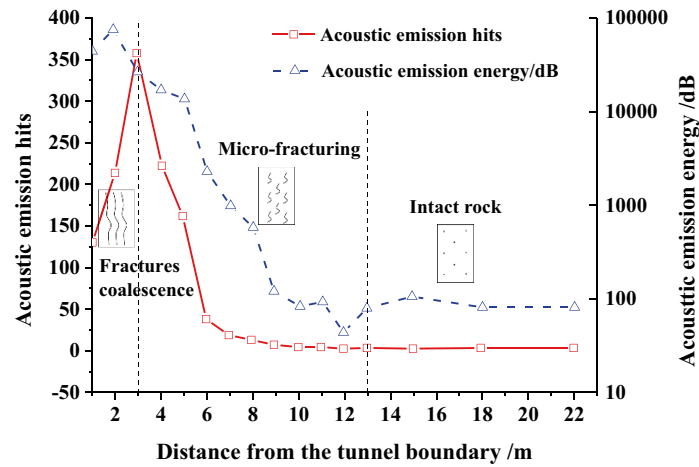
Fig. 34 Relationship between evolutionary characteristics of EDZ cracks and TBM driving: **a** position of TBM face on the measurement date: (1) TF01, $S = -46.85$ m, 7 days before excavation (December 5, 2009); (2) TF02, $S = 24.93$ m, 2 days before excavation (December 10, 2009); (3) TF03, $S = 47.33$ m, 3 days after excavation (December 15, 2009); and (4) some cracks gradually closed at TF04, $S = 208.42$ m, 15 days after excavation and tunnel supported (December 27, 2009), where S is the distance between the borehole section and the TBM excavation face. **(b)** Sketch map of crack evolution expressed by flattened patterns of the borehole SZ1-1 [65]



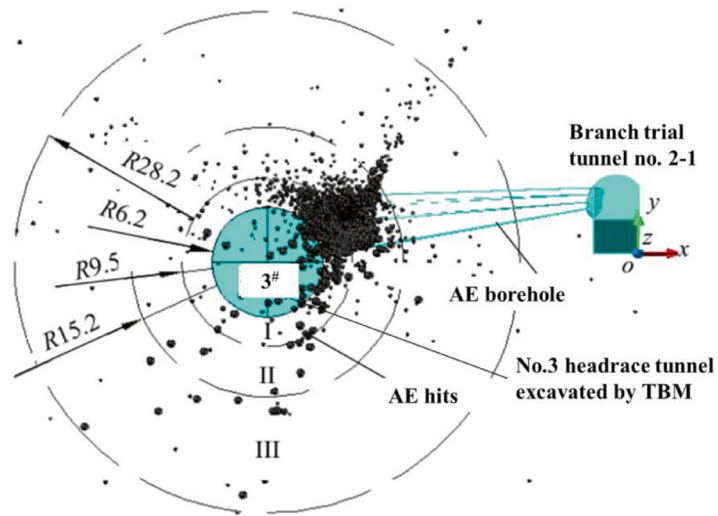
convergence gauge, multipoints multipoint extensometers, acoustic wave testing, digital borehole camera, acoustic emission (AE) monitoring, etc.

We have carried out field measurements for the convergence and inner displacement of the roadway surrounding rock in Huainan Panyidong coal mine (China). This is

Fig. 35 Damage evolution and the mechanism of surrounding rock along the radial direction of the tunnel during TBM excavation [66]. **a** Relationship between the acoustic emission hits and the surrounding rock damage-fracturing evolution, **b** the acoustic emission hits and the damage-fracture spatial distribution (unit: m)



(a) Relationship between the acoustic emission hits and the surrounding rock damage-fracturing evolution



(b) The acoustic emission hits and the damage-fracture spatial distribution (Unit: m)

a mechanized excavated roadway with the buried depth of 1020 m. Its main surrounding rock is sandy mudstone and that is where the rock samples were cored. Three monitoring stations were set up for the surrounding rock convergence and fracturing monitoring, as shown in Fig. 28. The in situ observation and monitoring results showed that the fractures were initiated, propagated and coalesced progressively, and finally a lot of macrocracks were generated near the roadway periphery, as shown in Fig. 29; the ruptured blocks slipped, rotated and shear dislocated with each other, which resulted in heavy convergence. The convergence and cracks also evolved with time. Consequently, the displacement at the roadway sidewall gradually increased to approximately 200 mm in 110 days (Fig. 30a), the floor heave grew to 300–500 mm in 75 days (Fig. 30b), and finally these convergences reached steady state; the

microfractures on the floor were initiated usually within 10 days after excavation and extended gradually, eventually growing into macrocracks and even big fissures (5–10 cm in width), as shown in Fig. 31. These results demonstrated that the surrounding rock went through evident damage, significant dilatancy, and fracture initiation, propagation and coalescence processes under excavation unloading; also the temporal effects were evident.

Li et al. [64, 65] performed the in situ measurements of fractures evolution within the excavation damaged zone (EDZ) in the TBM excavated No. 3 head race tunnel at Jinping II hydropower station (China) using a digital panoramic borehole camera, as shown in Fig. 32. The testing location is in the buried depth of 1900 m, and it was excavated in marble T_{2y}^5 (Yantang Group). The excavation diameter is 12.4 m. The changing relationships between the

fracturing process with the positions of the TBM face and testing time are presented, as shown in Figs. 33 and 34. The mechanism of fracture occurrence, formation and propagation with the TBM tunnelling process was researched in detail. The results showed that a large number of new small cracks were produced in the EDZ rock mass with a width of 2.0–8.0 mm during the TBM tunnelling process; some pre-existing joints and newly generated fractures experienced an evolutionary process of initiation, propagation, extension and closure during tunnel excavation and supporting. The excavation unloading condition and the stress redistribution were considered to be the main factors resulting in the surrounding rock fractures.

In addition, we carried out an in situ acoustic emission test on damage and fracture evolution of surrounding rock in LXB Water Diversion Tunnel (China) during TBM excavation. Chen et al. [66] also performed field acoustic emission monitoring for the disturbance and fracturing process in the TBM water diversion tunnels at Jinping II hydropower station (China). Both of the results showed that the surrounding rock underwent damage, dilatancy and fracturing processes, as shown in Fig. 35.

The revealed dilatancy and fracture evolution process in this study is in accordance with the above field observations and in situ monitoring data.

6 Conclusions

Triaxial unloading confining pressure tests and triaxial unloading creep tests, which reflect the intrinsic characteristics of excavation methods, were carried out on sandy mudstone. Based on the test results, the dilatancy and fracturing behavior of soft rock is studied, and the corresponding deformation mechanism is revealed. The main conclusions are as follows.

According to the laboratory triaxial unloading confining pressure experimental results, the unloading rate effects are studied and the damage evolution laws presented. It is found that during the smooth quasi-static unloading process with mechanized tunneling, the rock experiences pre-peak damage–dilatancy, and the volumetric strain develops in the dilatancy direction. When the peak strength is reached, the rock breaks and slides along the existing penetrated fracture surfaces, producing small brittle falls once or twice. With continuous unloading the confining pressure, linear strain softening occurs along an approximately oblique line with a small gradient, and multistage secondary microcracks are produced during this process. The deviatoric stress–strain curve consists of an elastic regime, a pre-peak unloading damage–dilatancy phase, a post-peak brittle drop section, a linear strain softening stage accompanied by multistage microcracks and a residual strength regime.

The soft rock has obvious time-dependent properties. The essence of progressive failure with time is the damage accumulation and is accompanied by time-dependent crack expansion, which is called ‘time-dependent damage and fracturing’ in this study. When the deviatoric stress is larger and the experienced creep time longer, the unloading effect and creep characteristics are more apparent and are accompanied by obvious lateral dilatancy, eventually leading to significant creep–dilatancy. This demonstrates that the damage and plastic deformation produced by unloading and creep have significant influences on the subsequent mechanical behavior.

Deep soft surrounding ground deformation is mainly composed of two parts: (a) pre-peak damage–dilatancy and volumetric expansion due to post-peak fracture–bulking at the instant of excavation unloading; (b) creep–dilatancy caused by time-dependent damage and fracturing.

The in situ measurements and the previous studies about the surrounding rock convergence, fracturing and EDZ development have verified the above results of damage, dilatancy and fractures evolution processes.

Acknowledgements This work was financially supported by the National Basic Research Program of China (‘973’ Program, grant No. 2014CB046904 and No. 2015CB058102) and the National Natural Science Foundation of China (Grant No. 41602326). Their support is gratefully acknowledged.

References

1. Liu QS, Huang X, Gong QM et al (2016) Application and development of hard rock TBM and its prospect in China. *Tunn Undergr Space Technol* 57:33–46
2. Hoek E, Marinos P (2000) Predicting tunnel squeezing problems in weak heterogeneous rock masses. *Tunn Tunn Int* 32(11):45–51; 32(12):34–36
3. Hoek E (2001) Big Tunnels in Bad Rock: The Thirty-Sixth Karl Terzaghi Lecture. *J Geotech Geoenviron* 127(9):726–740
4. Barla G (2002). Tunneling under squeezing rock conditions. In: *Advances in geotechnical engineering and tunnelling* (Kolymbas, D. (ed.)). Berlin: Logos Verlag, pp 169–268
5. Anagnostou G, Canti L (2007) Design and analysis of yielding support in squeezing ground. In: *The second half century of rock mechanics, 11th Congress of the International Society for Rock Mechanics (ISRM)*, Lisbon, vol 2. Taylor & Francis Group, London, pp 829–832
6. Ramoni M, Anagnostou G (2006) On the feasibility of TBM drives in squeezing ground. *Tunn Undergr Space Technol* 21(3): 262
7. Ramoni M, Anagnostou G (2010) Thrust force requirements for TBMs in squeezing ground. *Tunn Undergr Space Technol* 25(4):433–455
8. Shalabi FI (2005) FE analysis of time-dependent behavior of tunneling in squeezing ground using two different creep models. *Tunnelling Underground Space Technol* 20:271–279
9. Aristorenas GV (1992) Time-dependent behavior of tunnels excavated in shale. Ph. D. Dissertation, Massachusetts Institute of Technology

10. Ramoni M (2010) On the feasibility of TBM drives in squeezing ground and the risk of shield jamming. Ph. D. Dissertation, ETH Zurich
11. Aydan Ö, Akagi T, Kawamoto T (1996) The squeezing potential of rocks around tunnels: theory and prediction with examples taken from Japan. *Rock Mech Rock Eng* 29(3): 125–143.
12. Malan DF (2002) Simulating the time-dependent behavior of excavations in hard rock. *Rock Mech Rock Eng* 35(4): 225–254
13. Kolymbas D, Fellin W, Kirsch A (2006) Squeezing due to stress relaxation in foliated rock. *Int J Numer Anal Met* 30(13):1357–1367
14. Gharouni-Nik M, Fathali M (2013) Investigating the effect of dilation on VNL and CNL types shear strength. *Int J Civ Eng* 11(1):65–70
15. Qiu SL, Feng XT, Xiao JQ, Zhang CQ (2014) An experimental study on the pre-peak unloading damage evolution of marble. *Rock Mech Rock Eng* 47(2): 401–419
16. Li XZ, Shao ZS (2016) Investigation of macroscopic brittle creep failure caused by microcrack growth under step loading and unloading in rocks. *Rock Mech Rock Eng* 49(7):2581–2593
17. Martin CD, Kaiser PK, Christiansson R (2003) Stress, instability and design of underground excavations. *Int J Rock Mech Min Sci* 40(7–8):1027–1047
18. Huang RQ, Huang D (2014) Evolution of rock cracks under unloading condition. *Rock Mech Rock Eng* 47(2):453–466
19. Walton G, Arzúa J, Alejano LR, Diederichs MS (2015) A laboratory-testing-based study on the strength, deformability, and dilatancy of carbonate rocks at low confinement. *Rock Mech Rock Eng* 48(3):941–958
20. Dob H, Messast S, Mendjel A et al (2016) Behavior of sand after a high number of cycles application to shallow foundation. *Int J Civ Eng* 14(7):459–465
21. Bridgman PW (1950) Volume changes in the plastic stages of simple compression. *J Appl Phys* 20(12):1241–1251
22. Zhang K, Zhou H, Shao, JF (2013) An experimental investigation and an elastoplastic constitutive model for a porous rock. *Rock Mech Rock Eng* 46(6): 1499–1511
23. Kaiser PK, Yazici S, Maloney S (2001) Mining-induced stress change and consequences of stress path on excavation stability—a case study. *Int J Rock Mech Min Sci* 38(2):167–180
24. Cantieni L, Anagnostou G (2009) The effect of the stress path on squeezing behavior in tunneling. *Rock Mech Rock Eng* 42(2): 289–318
25. Moghaddas Tafreshi SN, Tavakoli Mehrjardi G, Ahmadi M (2011) Experimental and numerical investigation on circular footing subjected to incremental cyclic loads. *Int J Civ Eng* 9(4):265–274
26. Chen J, Jiang DY, Ren S, Yang CH (2016) Comparison of the characteristics of rock salt exposed to loading and unloading of confining pressures. *Acta Geotech* 11(1):221–230
27. Borhani A, Fakharian K (2016) Effect of particle shape on dilative behavior and stress path characteristics of chamkhaleh sand in undrained triaxial tests. *Int J Civ Eng* 14(4):197–208
28. Eberhardt E (2001) Numerical modelling of three-dimension stress rotation ahead of an advancing tunnel face. *Int J Rock Mech Min Sci* 38(4):499–518
29. Martin CD (1997) Seventeenth Canadian Geotechnical Colloquium: The effect of cohesion loss and stress path on brittle rock strength. *Can Geotech J* 34(5):698–725
30. Cai M, Kaiser PK (2005) Assessment of excavation damaged zone using a micromechanics model. *Tunn Undergr Space Technol* 20(4):301–310
31. Chen HF (2005) *Elasticity and Plasticity*. China Architecture & Building Press, Beijing
32. Tran-Manh H, Sulem J, Subrin D (2016) Progressive degradation of rock properties and time-dependent behavior of deep tunnels. *Acta Geotech* 11(3):693–711
33. Shao JF, Zhu QZ, Su K (2003) Modeling of creep in rock materials in terms of material degradation. *Comput Geotech* 30(7):549–555
34. Zhao YL, Cao P, Wang WJ et al (2009) Viscoelasto-plastic rheological experiment under circular increment step load and unload and nonlinear creep model of soft rocks. *J Cent South Univ Technol* 16(3):488–494
35. Debernardi D, Barla G (2009) New viscoplastic model for design analysis of tunnels in squeezing conditions. *Rock Mech Rock Eng* 42(2): 259–288
36. Wang GJ, Zhang L, Zhang YW, Ding GS (2014) Experimental investigations of the creep–damage–rupture behavior of rock salt. *Int J Rock Mech Min Sci* 66(1):181–187
37. Cai M (2008) Influence of stress path on tunnel excavation response-numerical tool selection and modeling strategy. *Tunn Undergr Space Technol* 23(6):618–628
38. Yan P, Lu WB, Chen M, Shan ZG, Chen XR, Zhou Y (2012) Energy release process of surrounding rocks of deep tunnels with two excavation methods. *J Rock Mech Geotech Eng* 4(2):160–167
39. Ji F, Lu JF, Shi YC, Zhou CH (2013) Mechanical response of surrounding rock of tunnels constructed with the TBM and drill-blasting method. *Nat Hazards* 66(2):545–556
40. Barton NR (2000) TBM tunneling in jointed and faulted rock. Balkema, Rotterdam
41. Yan P, Lu WB, Chen M et al (2012) Energy release process of surrounding rocks of deep tunnels with two excavation methods. *J Rock Mech Geotech Eng* 4(2):160–167
42. Liu J, Li JL, Wang XH, Qu JJ, Zhu T (2009) Study on unloading rock mass constitutive relationship. *Advances in Environmental Geotechnics, Proc. of Int Symp on Geoenvironmental Eng, ISGE* pp 480–486
43. Zhang QB, Zhao J (2014) Quasi-static and dynamic fracture behavior of rock materials: phenomena and mechanisms. *Int J Fract* 189(1):1–32
44. Ulusay R, Hudson JA (2007) The complete ISRM suggested methods for rock characterization, testing and monitoring: 1974–2006. Compilation arranged by the ISRM Turkish National Group, Ankara, Turkey
45. Marsden JE, Hughes TJR (1994) *Mathematical Foundations of elasticity*. Dover Publications, New York
46. Sharan SK (2008) Analytical solutions for stresses and displacements around a circular opening in a generalized Hoek-Brown rock. *Int J Rock Mech Min Sci* 40(1):78–85
47. Zhao XG, Wang J, Cai M et al (2014) Influence of unloading rate on the strainburst characteristics of beishan granite under true-triaxial unloading conditions. *Rock Mech Rock Eng* 47(2):467–483
48. Huang RQ, Wang XN, Chan LS (2001) Triaxial unloading test of rocks and its implication for rock burst. *Bull Eng Geol Env* 60(1): 37–41
49. Luo CW, Li HB, Liu YQ (2011) Characteristics of in-situ stress and variation law of plastic zone of surrounding rocks around deep tunnels in a coal mine. *Chin J Rock Mech Eng* 30(8): 1613–1618 (in Chinese)
50. Liu QS, Liu KD (2012) Characteristics of in-situ stress field for deep levels in Huainan coal mine. *Rock Soil Mech* 33(7): 2089–2096 (in Chinese)
51. Wu XY (1996) Stress relaxation, strain hardening and strain softening in rocks. *Prog Geophys* 11(4): 71–76 (in Chinese)
52. Zhang K, Zhou H, Pan PZ et al (2010) Characteristics of strength of rocks under different unloading rates. *Rock Soil Mech* 31(7): 2072–2078 (in Chinese)

53. Barla G, Debernardi D, Sterpi D (2012) Time-dependent modeling of tunnels in squeezing conditions. *Int J Geomech* 12(6):697–710
54. Barla G, Barla M, Bonini M, Debernardi D (2014) Guidelines for TBM tunneling in squeezing conditions—a case study. *Geotech Lett* 4: 83–87
55. Cao P, Wen YD, Wang YX et al (2016) Study on nonlinear damage creep constitutive model for high-stress soft rock. *Environ. Earth Sci* 75(10):1–8. doi:10.1007/s12665-016-5699-x
56. Kachanov LM (1986) Introduction to continuum damage mechanics, Martinus Nijhoff Publishers
57. Bonini M, Debernardi D, Barla M, Barla G (2009) The mechanical behavior of clay shales and implications on the design of tunnels. *Rock Mech Rock Eng* 42(2): 361–388
58. Sterpi D, Gioda G (2009) Visco-plastic behavior around advancing tunnels in squeezing rock. *Rock Mech Rock Eng* 42(2): 319–339
59. Hasanpour R, Rostami J, Ünver B (2014) 3D finite difference model for simulation of double shield TBM tunneling in squeezing grounds. *Tunn Undergr Space Technol* 40(2):109–126
60. Zhao K, Janutolo M, Barla G (2012) A completely 3D model simulation of mechanized tunnel excavation. *Rock Mech Rock Eng* 45(4): 475–497
61. Zhao K, Mariacristina B, Debernardi D, Janutolo M, Barla G et al (2015) Computational modelling of the mechanised excavation of deep tunnels in weak rock. *Comput Geotech* 66:158–171
62. Munjiza A (2004) The Combined Finite-Discrete Element Method. John Wiley & Sons Ltd, London
63. Shi GH (1991) Manifold method of material analysis. Paper presented at the Trans 9th Army conference on applied mathematics and computing, Minneapolis: Minesota
64. Li SJ, Feng XT, Li ZH et al (2011) In situ experiments on width and evolution characteristics of excavation damaged zone in deeply buried tunnels. *Sci China* 54(S1): 167–174.
65. Li SJ, Feng XT, Li ZH et al (2012) Evolution of fractures in the excavation damaged zone of a deeply buried tunnel during TBM construction. *Int J Rock Mech Min Sci* 55:125–138
66. Chen BR, Feng XT, Xiao YX et al (2010) Acoustic emission test on damage evolution of surrounding rock in deep-buried tunnel during TBM excavation. *Chin J Rock Mech Eng* 29(8): 1562–1569 (in Chinese)